Manuscript prepared for Atmos. Chem. Phys.
with version 3.2 of the LaTeX class copernicus.cls.
Date: 30 November 2012

Supplement to: A new multi-gas constrained model of trace gas non-homogeneous transport in firn: evaluation and behavior at eleven polar sites

E. Witrant[1], P. Martinerie[2], C. Hogan[3], J. C. Laube[3], K. Kawamura[4,5], E. Capron[6,7], S. A. Montzka[8], E. J. Dlugokencky[8], D. Etheridge[9], T. Blunier[10], and W. T. Sturges[3]

[1]UJF-Grenoble 1/CNRS, Grenoble Image Parole Signal Automatique (GIPSA-lab), UMR5216, B.P. 46, 38402 St Martin d'Hères, France
[2]UJF-Grenoble 1/CNRS, Laboratoire de Glaciologie et Géophysique de l'Environnement (LGGE) UMR5183, Grenoble, 38041, France
[3]School of Environmental Sciences, University of East Anglia, Norwich NR4 7TJ, UK
[4]National Institute of Polar Research, 10-3 Midorichou, Tachikawa, Tokyo 190-8518, Japan
[5]Institute of Biogeosciences, Japan Agency for Marine-Earth Science and Technology, 2-15 Natsushima-cho, Yokosuka 237-0061, Japan
[6]Laboratoire des Sciences du Climat et de L'Environnement, IPSL/CEA-CNRS-UVSQ, 91191 Gif-sur-Yvette, France
[7]British Antarctic Survey, Natural Environment Research Council, High Cross, Madingley Road, Cambridge CB3 0ET, UK
[8]NOAA Earth System Research Laboratory, Boulder, Colorado, USA
[9]Commonwealth Scientific and Industrial Research Organisation, Marine and Atmospheric Research, PMB 1, Aspendale, Vic. 3195, Australia
[10]Centre for Ice and Climate, Niels Bohr Institute, University of Copenhagen, Juliane Maries VEJ 30, 2100 Copenhagen Ø, Denmark

1 Forward model of gas transport in firn

The notations chosen for the main physical variables are presented in Table 1. The subscript α is generally used for trace gases while the superscripts o or c indicate the considered quantity in the open or closed porosity network, respectively. The first and second partial derivatives with respect to space are indicated with $[\cdot]_z$ and $[\cdot]_{zz}$, respectively, and the one with respect to time as $[\cdot]_t$.

1.1 Model equivalencies

Our proposed transport model is:

$$\begin{cases} [\rho_\alpha^o f]_t + [\rho_\alpha^o f(v+w_{\rm air})]_z + \rho_\alpha^o(\tau+\lambda) = \\ \quad \left[D_\alpha\left([\rho_\alpha^o]_z - \rho_\alpha^o \dfrac{M_{\alpha/{\rm air}}g}{RT}\right)\right]_z \\ \rho_\alpha^o(0,t) = \rho_\alpha^{\rm atm}(t) \\ \dfrac{RT}{M_\alpha g}[\rho_\alpha^o(z_{\rm F},t)]_z - \rho_\alpha^o(z_{\rm F},t) = 0 \end{cases} \tag{1}$$

where:

$$M_{\alpha/{\rm air}} = \begin{cases} M_{\rm air} & \text{if} \quad z \le z_{conv} \\ M_\alpha & \text{if} \quad z > z_{conv} \end{cases} \tag{2}$$

Eq. (1) is expressed in terms of gas concentration as it was established from mass conservation. This allows for a direct relationship with the transport terms definition. While keeping the concentration as the main variable can be useful for a robust algorithm implementation, it is interesting to change the state variable in order to compare with other published firn models. Note that the radioactive decay term was not included (contrarily to the model in the main paper) to simplify the comparison and could simply be introduced as a mass loss on ρ_α^o)

1.1.1 Equivalence with a formulation in amount of gas

Defining the gas quantity $q(z,t) = f(z) \times \rho_\alpha^o(z,t)$, Eq. (1) is equivalent to:

$$\begin{cases} q_t + [q(v+w_{\rm air})]_z + q\tau/f = \\ \qquad \left[D_\alpha\left([q/f]_z - q/f\dfrac{M_{\alpha/{\rm air}}g}{RT}\right)\right]_z \\ q(0,t) = f(0)\rho_\alpha^{\rm atm}(t) \\ \dfrac{RT}{M_\alpha g}[q(z_{\rm F},t)/f(z_{\rm F})]_z - q(z_{\rm F},t)/f(z_{\rm F}) = 0 \end{cases} \tag{3}$$

The model proposed by Rommelaere et al. (1997) is obtained from Eq. (3) below z_{conv} (the convective region was constructed by setting q as constant in the upper part) and $q(z_{\rm F},t) = 0$ (no gas in contact with the atmosphere in the last layer). When this model was used in a first attempt to calculate a multi-gas constrained diffusivity, some problems appeared due to the convective region (lack of accuracy in the upper part) and to numerical oscillations (bottom boundary condition and terms containing the inverse of f, which

Correspondence to: Emmanuel WITRANT
(emmanuel.witrant@ujf-grenoble.fr)

Table 1. Main physical variables

Notation	Physical variable and unit
a_{accu}	snow accumulation rate (kg/m^2/yr)
$c(z,t)$	mixing ratio (mol/mol)
c_f	correction factor on the diffusivity in air ($f(0)$)
$D(z)$	diffusivity (m^2/yr)
$D_\alpha(z)$	effective diffusivity of gas α in firn (m^2/yr)
$D_{\mathrm{eff}}(z)$	optimal effective diffusivity of CO_2 in firn (m^2/yr)
$D_{\alpha,\mathrm{air}}$	molecular diffusion coefficient of gas α in free air (m^2/yr)
$D_{\mathrm{CO_2,air}}$	molecular CO_2 diffusivity in free air (m^2/yr)
$D_{\mathrm{eddy}}(z)$	eddy component in effective diffusivity (m^2/yr)
$f(z)$	open porosity (m^3/m^3)
g	gravitational acceleration (9.81 m/s^2)
$M_{\mathrm{air}/\alpha}$	air/trace gas molar mass (kg/mol)
$m(z)$	measured mixing ratio (mol/mol)
N_g	number of trace gases
N_m	number of measurements
$P(z)$	pressure in open pores (Pa)
$P_{\mathrm{atm,co}}$	atmospheric and mean close-off pressure (Pa)
P_0	reference atmospheric pressure (101325 Pa)
$Pe(z,t)$	Péclet number
$q(z,t)$	gas quantity in the open pores volume (mol/m^3 of open pores volume)
$r^{x\to y}(z)$	rate of fluid mass transfer from x to y (mol/m^3/yr)
r_α	relative diffusivity of gas α with respect to D_{air}
R	ideal gas constant (8.314 J/mol/K)
RMSD	root mean square deviation
R_{std}	standard molar ratio for δ computation (mol/mol)
T	firn temperature (K)
$T_{0,\mathrm{co}}$	reference (273) and mean close-off temperature (K)
t_{F}	measurement date (yr)
V_{co}	parameterized close-off porous volume (cm^3/g)
V	air content obtained from the experimental parameterization (cm^3/g)
$v(z)$	firn sinking velocity (m/yr)
$w_{\mathrm{gas/air}/\alpha}(z,t)$	relative gas/air/trace gas advection velocity with respect to firn (m/yr)
$\bar{w}_{\mathrm{air}/\alpha}(z)$	air/trace gas advection velocity with respect to firn at steady-state (m/yr)
z	depth location in the firn (m)
z_{F}	full close-off depth (m)
$\delta(z,t)$	δ-ratio of gas isotopes (‰)
Δz	depth increment between model layers (m)
$\Delta w_\alpha(z,t)$	trace gas velocity in air induced by molecular diffusion (m/yr)
$\Delta\bar{w}_\alpha(z,t)$	steady-state trace gas velocity in air (m/yr)
$\epsilon(z)$	total porosity (m^3/m^3)
$\kappa(z)$	permeability (m^2)
λ	radioactive decay rate (yr^{-1})
$\nu(z)$	firn tortuosity
$\Phi(z,t)$	mixing ratio flux (mol/mol/m/yr)
χ_x	mole fraction of gas x (trace gas or air) in the gas mixture
$\rho_{\mathrm{firn/ice/co}}(z)$	firn/ice/close-off density versus depth (kg/m^3 of void space)
$\rho^o_{\mathrm{gas/air}/\alpha}(z,t)$	gas/air/trace gas concentration in open pores (mol/m^3 of void space)
$\rho^c_{\mathrm{gas/air}/\alpha}(z,t)$	gas/air/trace gas concentration in closed pores (mol/m^3 of void space)
$\rho^{\mathrm{atm}}_{\mathrm{air}/\alpha}(t)$	air/trace gas atmospheric concentration (mol/m^3 of void space)
$\bar{\rho}^o_{\mathrm{air}/\alpha}(z)$	air/trace gas concentration profile at steady-state (mol/m^3 of void space)
$\sigma(z)$	uncertainty on measured mixing ratios (mol/mol)
$\tau(z)$	rate of gas mass exchange between open and closed networks (yr^{-1})

goes to zero at the end of the close-off region, and its derivative). These problems motivated the initial model revision in terms of concentration and to clearly identify the nature and formulation of the different velocity components.

1.1.2 Equivalence with a formulation in gas mixing ratios, using a Lagrangian frame

The transport model (1) can be expressed in terms of gas mixing ratio $c(z,t)=\rho^{\mathrm{o}}_\alpha(z,t)/\rho_{\mathrm{air}}(z)$ by noticing that:

$$\rho^{\mathrm{o}}_\alpha = c\rho_{\mathrm{air}}, \quad [\rho^{\mathrm{o}}_\alpha]_z = \rho_{\mathrm{air}}[c]_z + [\rho_{\mathrm{air}}]_z c$$

and (air transport and trapping equilibrium):

$$[\rho_{\mathrm{air}} f(v+w_{\mathrm{air}})]_z + \rho_{\mathrm{air}}\tau = 0$$

The gas dynamics is then expressed in terms of mixing ratio as:

$$\frac{\partial c}{\partial t} + (v+w_{\mathrm{air}})[c]_z = \left(\frac{f_z}{f} + \frac{[\rho_{\mathrm{air}}]_z}{\rho_{\mathrm{air}}}\right)\Phi + [\Phi]_z \qquad (4)$$

with the mixing ratio flux:

$$\Phi(z,t) = \frac{D_\alpha}{f}\left([c]_z + \frac{(M_{\mathrm{air}} - M_{\alpha/\mathrm{air}})g}{RT}c\right)$$

Our model is set in an Eulerian frame (fixed with respect to the surface) and can be expressed in a Lagrangian coordinate (moving with particles that have a velocity $v+w_{\mathrm{air}}$ in the Eulerian frame) using the relationship:

$$\frac{dc}{dt} = \frac{\partial c}{\partial t} + (v+w_{\mathrm{air}})[c]_z$$

where d/dt denotes the Lagrangian derivative. The mixing ratio dynamics (4) is then equivalent to:

$$\frac{dc}{dt} = \left(\frac{f_z}{f} + \frac{[\rho_{\mathrm{air}}]_z}{\rho_{\mathrm{air}}}\right)\Phi + [\Phi]_z$$

and the air transport model (determined by firn sinking and air trapping) defines the absolute position (Eulerian frame) of the relative coordinates, which is necessary to relate the modeled mixing ratios to the firn measurements. Comparing this expression with the model proposed by Trudinger et al. (1997), the equivalence is established (neglecting the radioactive decay and the impact of the air flow velocity) below z_{conv}. The main advantage of the Lagrangian framework is that it allows tracking surface alterations of the flux within the firn. Indeed, the snow melting process is thus modeled by Trudinger et al. (1997) as the sinking of a layer with reduced diffusivity. Such a phenomenon could be mapped in the Eulerian framework by defining a time-varying diffusivity, parameterized in terms of the firn sinking velocity. However, it involves in both cases the use of finer numerical schemes (and hence larger simulation times) that are not compatible with the proposed multi-gas optimization goal.

1.1.3 Equivalence with an isotopic ratio formulation

Isotopic ratios are variables of particular interest for the study of inert gases. When an isotopic ratio is mostly constant in the atmosphere, its values in firn can be used, for example, to compare the timing of greenhouse gas changes versus climate (Severinghaus et al., 1998). The behavior of an isotopologue 1 with respect to isotopologue 2 is typically expressed with the δ notation:

$$\delta = \left(\frac{\rho_1/\rho_2}{R_{\mathrm{std}}} \frac{M_2}{M_1} - 1 \right) \times 10^3 \tag{5}$$

where δ is expressed in ‰, R_{std} is the standard molar ratio for the gases considered (constant scalar variable), $\rho_{1,2}$ are the concentrations in air and the ratio of molar masses M_2/M_1 is introduced to express the mass ratio in terms of a molar ratio.

If ρ_1 and ρ_2 are both considered to vary with time and depth, the computation of δ implies to solve the transport equations (1) for both isotopes in air in parallel and then obtain their ratio. If 2 is considered as a dominant gas that has a constant concentration with respect to time and is transported with air, a compact expression can be obtained for δ. First, setting $[\rho_2]_t = 0$ implies that (4) writes equivalently as (considering the transport in gas 2 instead of air):

$$f\rho_2([\chi_{1,2}]_t + (v + w_{air})[\chi_{1,2}]_z) = \left[\rho_2 D_{1,2} \left([\chi_{1,2}]_z + \frac{(M_2 - M_{1/2})g}{RT} \chi_{1,2} \right) \right]_z$$

where $D_{1,2}$ is the diffusivity of gas 1 in gas 2. Then, expressing $\chi_{1,2}$ and its partial derivatives in terms of δ provides the dynamics:

$$\begin{aligned} & f[\delta]_t + f(v + w_{\mathrm{air}})[\delta]_z \\ &= \frac{1}{\rho_2} \left[\rho_2 D_{1,2} \left([\delta]_z + \frac{(M_2 - M_{1/2})g}{RT} (\delta/1000 + 1) \right) \right]_z \\ &= \left[D_{1,2} \left([\delta]_z + \frac{(M_2 - M_{1/2})g}{RT} (\delta/1000 + 1) \right) \right]_z \\ &\quad + \frac{[\rho_2]_z}{\rho_2} \left[D_{1,2} \left([\delta]_z + \frac{(M_2 - M_{1/2})g}{RT} (\delta/1000 + 1) \right) \right] \end{aligned}$$

This transport model can be compared with the one proposed by Severinghaus et al. (2010). Both models are equivalent if: (1) the last term (involving $[\rho_2]_z$) is neglected; (2) an eddy diffusion term is added specifically to the flux associated with $[\delta]_z$; (3) the steady-state equilibrium is set with an additional term that depends on the thermal gradient and on the thermal diffusion sensitivity.

A new isotopic ratio model that does not necessitate the steady-state hypothesis for the major isotope and takes into account all the terms involved by the transport equations (1) is provided in Witrant and Martinerie (2013).

1.2 Bulk air transport and bubble trapping

A direct approach to calculate the air transport velocity would require a knowledge of the firn permeability (scaling laws such as those proposed by Schwander (1989) or Freitag et al. (2002) could be used for this purpose) to compute the advective flow. As discussed in the main paper, an alternative is to use the continuity equation and the hydrostatic equilibrium of air concentration to obtain the bulk air transport velocity as the solution of the linear boundary value problem:

$$[\bar{\rho}^{\mathrm{o}}_{\mathrm{air}} f v]_z + [\bar{\rho}^{\mathrm{o}}_{\mathrm{air}} f w_{\mathrm{air}}]_z = -\bar{\rho}^{\mathrm{o}}_{\mathrm{air}} \tau, \quad w_{\mathrm{air}}(z_{\mathrm{f}}) = 0$$

The advantage of this approach (previously used by Rommelaere et al., 1997) is to provide $w_{\mathrm{air}}(z)$ without the momentum conservation equation but the drawback is to necessitate a hydrostatic profile for the air concentration. This may be a strong hypothesis in the gas trapping region, where neglected local pressure gradients (e.g. induced by surface stress and capillary pressure, see Coussy, 2003) may alter the natural hydrostatic pressure distribution. Nevertheless, we consider the hydrostatic air distribution as a necessary condition for the direct model, and the solution of the BVP is:

$$w_{\mathrm{air}}(z) = \frac{1}{\bar{\rho}^{\mathrm{o}}_{\mathrm{air}}(z) f(z)} \int_z^{z_{\mathrm{f}}} (\bar{\rho}^{\mathrm{o}}_{\mathrm{air}} \tau + [\bar{\rho}^{\mathrm{o}} f v]_z) dz$$

The air trapped in closed pores $\rho^{\mathrm{c}}_{\mathrm{air}}$ is directly obtained from Eq. (1c) of the main paper at steady-state as:

$$[\rho^{\mathrm{c}}_{\mathrm{air}}(\epsilon - f)v]_z = \rho^{\mathrm{o}}_{\mathrm{air}} \tau, \quad \rho^{\mathrm{c}}_{\mathrm{air}}(0) = \rho^{\mathrm{atm}}_{\mathrm{air}}$$

with $\rho^{\mathrm{o}}_{\mathrm{air}} \approx \bar{\rho}^{\mathrm{o}}_{\mathrm{air}}$ and can be evaluated by the air content computation:

$$\text{Air Content} = \frac{q^{\mathrm{c}}_{\mathrm{air}}}{\rho^{\mathrm{atm}}_{\mathrm{air}}} \frac{1}{\rho_{\mathrm{firn}}} = \frac{\epsilon - f}{1 - \epsilon} \frac{\rho^{\mathrm{c}}_{\mathrm{air}}}{\rho^{\mathrm{atm}}_{\mathrm{air}}} \frac{1}{\rho_{\mathrm{ice}}}$$

where $q^{\mathrm{c}}_{\mathrm{air}}$ denote the molar concentrations of air in the closed pores volume. The modeled air content can be compared to experimental data (e.g. in Martinerie et al., 1994).

On the upper left panel of Figure 1, our modeled values of air content in ice are compared with parameterized values calculated as:

$$V^{\mathrm{ref}}_{\mathrm{co}} = 6.9510^{-4} T_{\mathrm{co}} - 0.043 \tag{6a}$$

$$V = V^{\mathrm{ref}}_{\mathrm{co}} \frac{P_{\mathrm{co}}}{T_{\mathrm{co}}} \frac{273}{1013} \tag{6b}$$

where $V^{\mathrm{ref}}_{\mathrm{co}}$ is the parameterized close-off porous volume from Martinerie et al. (1994), V is the air content (see e.g. Martinerie et al., 1992) obtained from $V^{\mathrm{ref}}_{\mathrm{co}}$, T_{co} and P_{co} are the temperature and pressure at mean close-off depth. Although the order of magnitude of modeled air content values is correct, the values for individual sites are much more dispersed around the parameterized values from Eq. (6) than the experimental data in Martinerie et al. (1992). Air content is

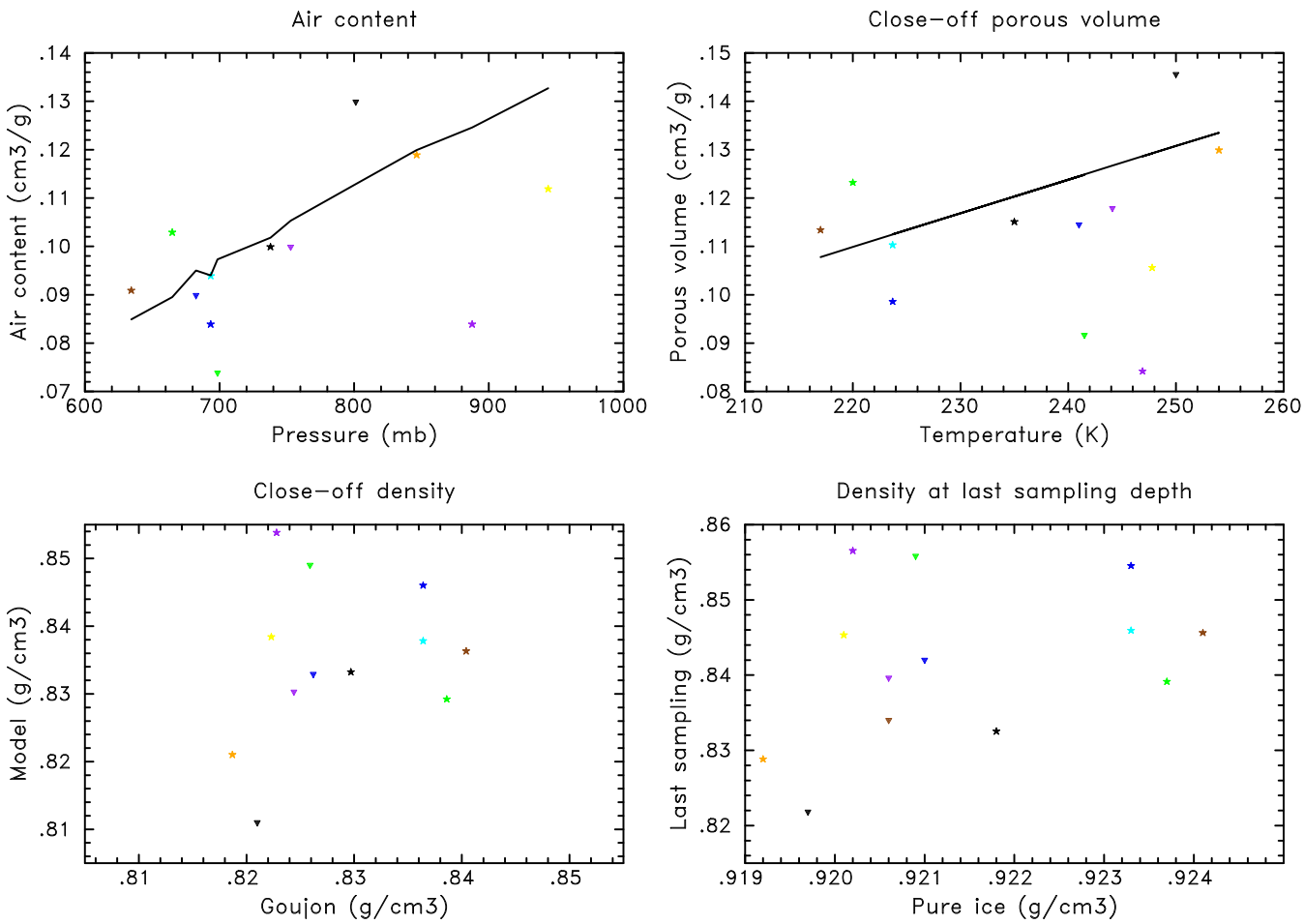

Fig. 1. Modeled air content in ice and related parameters. Upper left panel: comparison of modeled air content (symbols) with parameterized values from Eq. (6) (plain line). Upper right panel: comparison of modeled mean close-off porosity (symbols) with parameterized values from Eq. (6a) (plain line). Lower left panel: modeled mean close-off density as a function of parameterized values from Goujon et al. (2003). Lower right panel: density at last sampling depth as a function of pure ice density. Site representation - Devon Island: black triangles, Summit: blue triangles, NEEM-EU: purple triangles, NEEM-US: brown triangles (masked by the superimposed NEEM-EU except on lower right panel), North GRIP: green triangles, DE08: orange stars, Berkner: purple stars, Siple: yellow stars, South Pole 1995: dark blue stars, South Pole 2001: light blue stars, Dronning Maud Land: black stars, Dome C: green stars and Vostok: brown stars.

primarily dependent on the atmospheric pressure of the firn drilling site, which is an input parameter of the model rather than a calculated variable. Thus the upper right panel of Figure 1 compares our model results of mean close-off porous volume (V_{co}) with parameterized values from Eq. (6a). Site to site variations of V_{co} are more directly dependent on model variables (such as the depth profile of closed porosity) than V. However the model results for V and V_{co} on Figure 1 show very similar positive and negative anomalies around parameterized values.

The mean close-off density (ρ_{co}) is directly related to V_{co}: $1/\rho_{\mathrm{co}} = V_{\mathrm{co}} + 1/\rho_{\mathrm{ice}}$ (ρ_{ice} being the density of pure ice). Modeled values of ρ_{co} can be plotted as a function of the density at the model depth level where the closed porosity is 37% of the total porosity (mean close-off density as defined in Goujon et al., 2003). The results, shown on the lower left panel of Figure 1, should ideally be aligned on the diagonal of the plot. Large anomalies of similar nature are obtained again: as V_{co} is proportional to $1/\rho_{\mathrm{co}}$, positive anomalies on the upper panels of Figure 1 become negative anomalies on the lower panels and vice versa.

Finally, the density at the last firn sampling depth (a parameter which is independent from the model physics) shows similar anomalies when plotted as a function of ρ_{ice} (lower right panel of Figure 1). We thus interpret the anomalies on Figure 1 as due to scale differences in our density profiles. High density values (fairly close to the density of pure ice) are difficult to measure precisely for at least two reasons: the temperature of the ice core should be controlled precisely to ensure the consistency between ρ_{firn} and ρ_{ice}, and the ice

core volume measurements can be biased if the core shape is irregular (see also Section 3.1).

1.3 Discretization of the transport equation

1.3.1 Background on the discretization of PDEs

The proposed trace gas transport model belongs to the general class of models described by:

$$\begin{aligned}&[q]_t = \mathcal{D}[q]_{zz} + \mathcal{C}[q]_z + \mathcal{S}q\\&q(0,t) = q_0(t), \quad k_1[q]_z(z_{\mathrm{F}},t) + k_2 q(z_{\mathrm{F}},t) = 0\end{aligned}$$

where $q(z,t)$ is a generic transported variable, $\mathcal{S}(z)$ a sink term and k_1 and k_2 ensure that the net flux at z_{F} (location of the end boundary condition, e.g. bottom of the firn) is zero. The transport coefficients $\mathcal{D}(z)$ and $\mathcal{C}(z)$, associated with the second and first spacial derivatives, are referred to as *diffusion* and *convection*, respectively. This distinction, instead of the physical diffusive and advective transport used previously, is motivated by the specificities of the associated mathematical aspects and numerical schemes.

The discretized model is set by introducing $Q^k = [Q_1^k \dots Q_i^k \dots Q_N^k]^T \in \mathbb{R}^{N\times 1}$ as the vector of discretized $q(z,t)$ at the space locations z_i and the time instant t_k. The resulting variation law for depth i (considering an implicit time discretization scheme, for example) is:

$$\begin{aligned}Q_i^{k+1} = Q_i^k + t_s\big[&\mathcal{D}_i D(Q_{i-1},Q_i,Q_{i+1})^{k+1}\\&+C(Q_{i-1},Q_i,Q_{i+1},\mathcal{C}_i)^{k+1} + \mathcal{S}_i Q_i^{k+1}\big]\end{aligned}$$

where t_s is the sampling time and $D(\cdot)$ and $C(\cdot)$ are the discretization operators for diffusion and convection, respectively.

The space-discretization can be achieved, for example, with a central difference scheme for D and a Lax-Wendroff (LW) scheme for C (the model thus remains stable for $\mathcal{D}(z) = 0$ provided that the Courant-Friedrichs-Lewy condition is satisfied). The choice of a LW scheme is also motivated by the improved accuracy for convection modeling (the numerical diffusion typically associated with a central or first order upwind scheme is thus avoided). Further details on the stability of the numerical schemes may be found in PDE or computational fluid dynamics textbooks, such as (Mattheij et al., 2005) or (Hirsch, 2007). According to this choice:

$$\begin{aligned}&D(Q_{i-1},Q_i,Q_{i+1})^{k+1} = (Q_{i-1}^{k+1} - 2Q_i^{k+1} + Q_{i+1}^{k+1})/\Delta z^2\\&C(Q_{i-1},Q_i,Q_{i+1},\mathcal{C}_i)^{k+1} =\\&\qquad \frac{\alpha_i}{t_s}\left(\frac{\alpha_i - 1}{2}Q_{i-1}^{k+1} - \alpha_i Q_i^{k+1} + \frac{\alpha_i+1}{2}Q_{i+1}^{k+1}\right)\end{aligned}$$

where Δz is the spatial step and $\alpha_i = \mathcal{C}_i t_s/\Delta z$.

Considering the fact that the transport coefficients are assumed to be constant in time and introducing the time-varying boundary condition on $q(0,t)$ with the vector $Q_0^k = [q_0^k\ 0 \dots 0]^T \in \mathbb{R}^{N\times 1}$, the discretized model writes in the matrix form:

$$\begin{aligned}&Q^{k+1} = Q^k + t_s\left[\mathcal{A}Q^{k+1} + \mathcal{B}Q_0^{k+1}\right]\\&\Leftrightarrow Q^{k+1} = (I/t_s - \mathcal{A})^{-1}[I/t_s Q^k + \mathcal{B}Q_0^{k+1}]\end{aligned}$$

where $\mathcal{A} = \mathcal{A}_D + \mathcal{A}_{CS}$ and $\mathcal{B} = \mathcal{B}_D + \mathcal{B}_{CS}$. $\mathcal{A}_D$, $\mathcal{A}_{CS}$ are tri-diagonal matrices and $\mathcal{B}_D$, $\mathcal{B}_{CS}$ are vectors with entries:

$$\begin{aligned}&\mathcal{A}_{D,1} = \frac{\mathcal{D}_1}{\Delta z^2}[0,-2,1], \quad \mathcal{A}_{D,i} = \frac{\mathcal{D}_i}{\Delta z^2}[1,-2,1],\\&\mathcal{A}_{D,N} = \frac{\mathcal{D}_N}{\Delta z^2}[1,-1,0],\\&\mathcal{A}_{CS,1} = \frac{\alpha_1}{t_s}\left[0, -\alpha_1, \frac{\alpha_1+1}{2}\right] + \mathcal{S}_1,\\&\mathcal{A}_{CS,i} = \frac{\alpha_i}{t_s}\left[\frac{\alpha_i-1}{2}, -\alpha_i, \frac{\alpha_i+1}{2}\right] + \mathcal{S}_i,\\&\mathcal{A}_{CS,N} = \frac{\alpha_N}{t_s}\left[\frac{\alpha_N-1}{2}, \frac{-\alpha_N+1}{2}, 0\right] + \mathcal{S}_N,\\&\mathcal{B}_{D,1} = \frac{\mathcal{D}_1}{\Delta z^2}[1], \quad \mathcal{B}_{CS,1} = \frac{\alpha_1}{t_s}\left[\frac{\alpha_1-1}{2}\right]\end{aligned}$$

where $[\cdot,\cdot,\cdot]$ is a line vector with three entries, centered at the i index (used as both line and column indexes)

This space-discretization can also be used in an explicit time-discretization scheme for specific purposes, in which case:

$$\begin{aligned}&Q^{k+1} = Q^k + t_s\left[\mathcal{A}Q^k + \mathcal{B}Q_0^k\right]\\&\Leftrightarrow Q^{k+1} = t_s[(I/t_s + \mathcal{A})Q^k + \mathcal{B}_D Q_0^k]\end{aligned}$$

Hybrid explicit/implicit schemes (such as Crank-Nicolson if the weight of each is equivalent) may also be devised.

Note that for gases with constant atmospheric concentration $Q_0^k = Q_0$ is constant (no time-varying input in the model) and the concentration profile is directly obtained (a time loop is unnecessary) as $Q = \mathcal{A}^{-1}\mathcal{B}Q_0$. This relationship is also used in the numerical model as an estimate of the initial condition, as it depicts the gas equilibrium in the firn if the atmospheric concentration remained constant for a "sufficiently long" period of time.

1.3.2 Impact of space discretization

The discretization schemes discussed in the previous section are illustrated on NEEM Greenland site (EU hole) with a multi-gases diffusivity calculated with 395 depth levels. All simulations were performed with the same diffusivity profile, obtained from the inverse diffusivity model set with a LW scheme sampled with $N = 395$ depths and atmospheric scenarios provided every month.

The impacts of the convection term discretization scheme and the number of discretization depths are presented in Figure 2, where LW, central and first-order upwind (FOU) discretizations are compared for three numbers of depths N. Concerning the effect of N, it appears that large differences

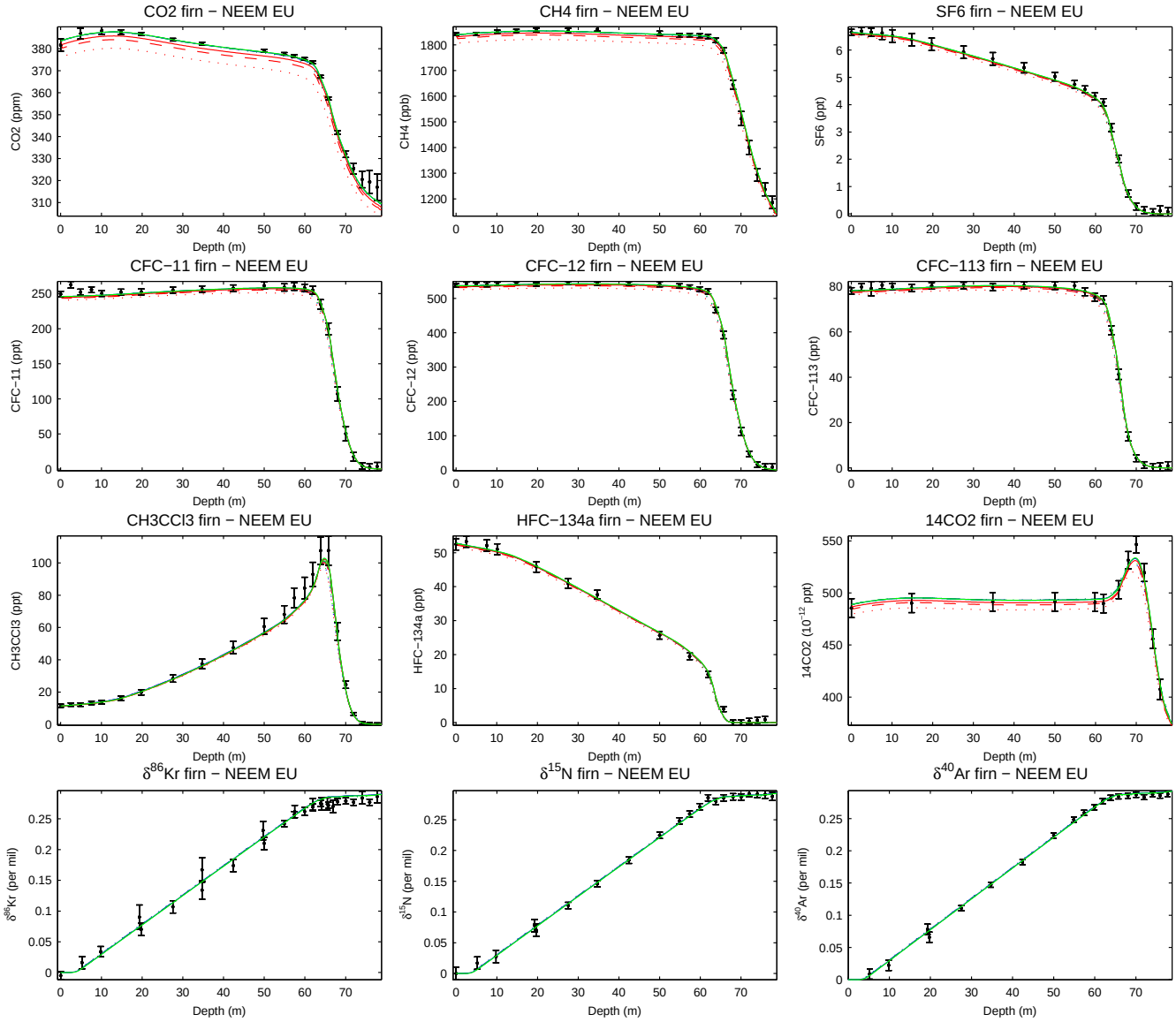

Fig. 2. Impact of the convection term discretization on the trace gas mixing ratios at NEEM (EU hole) for 100 (‘ $\cdots$ ’), 200 (‘- - -’) and 395 (‘—’) depth levels ($\Delta z \approx 0.8$, 0.4 and 0.2 m, respectively): Lax-Wendroff (blue, reference), central (red) and first order upwind (green).

occur between $N = 100$ and $N = 200$ but $N = 200$ provides a good approximation of the full resolution ($N = 395$). Concerning the convection term discretization scheme, central difference tends to be more sensitive to the space discretization. Only slight differences can be observed for $N = 395$ except for the gases with constant atmospheric concentrations, for which the central scheme induces an important mismatch at the upper BC (removed from the figure). The improvements of the central and FOU schemes on some gases (i.e. SF_6 and CH_3CCl_3) are balanced by an increased error on some others (i.e. CFCs and HFC-134a). This is directly related to the fact that the inverse diffusivity model involves a balance amongst all the gases and all the measurement depths. A different discretization scheme in the inverse diffusivity model would imply a different diffusivity profile, which inherently accounts for the numerical properties of the model.

Similar conclusions can be obtained on Antarctic sites (for example at Dome C, presented on Figure 3), where discrepancies can be observed with a central scheme, while FOU tends to increase the convective transport.

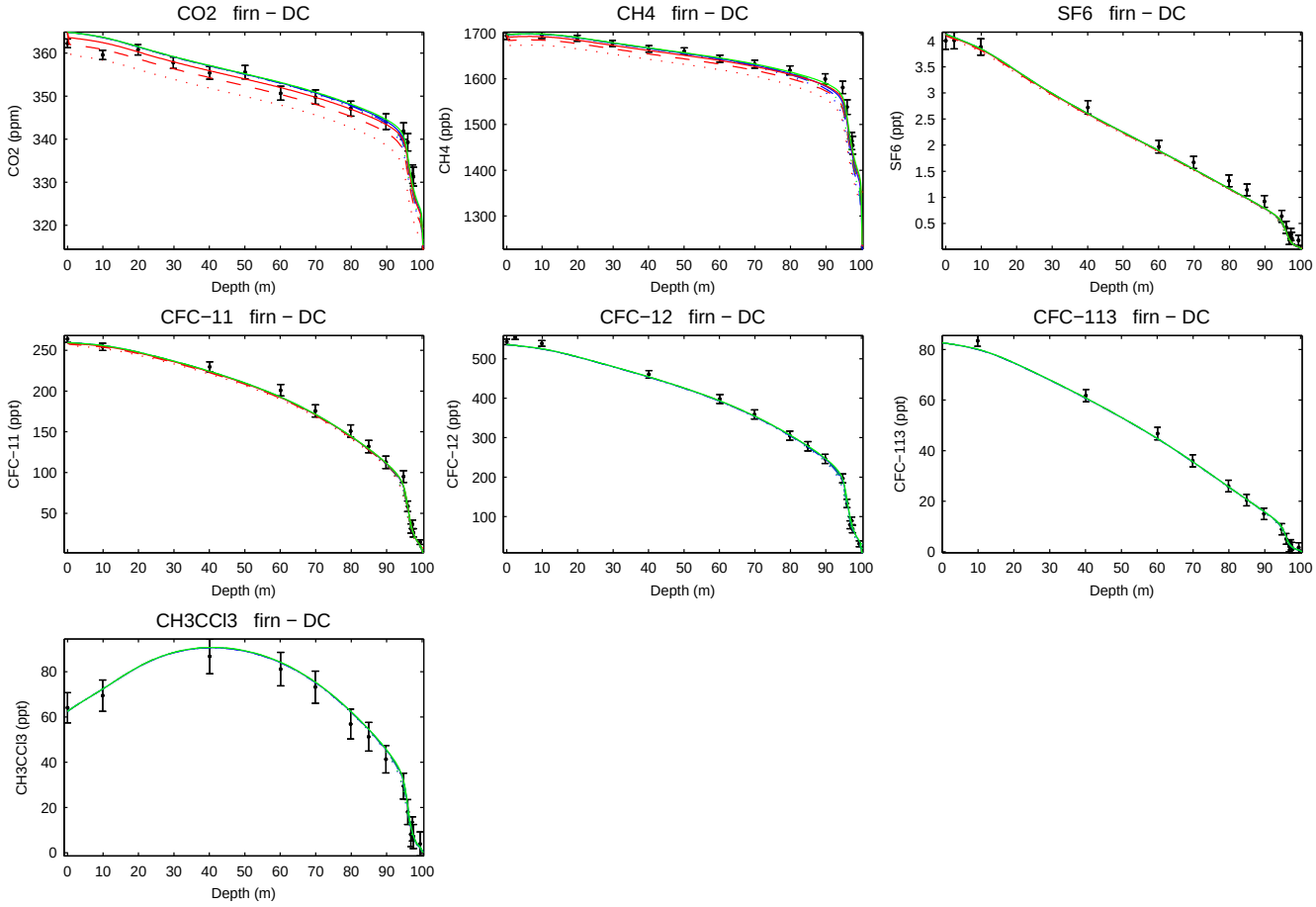

Fig. 3. Impact of the convection term discretization on the trace gas mixing ratios at Dome C for $N = 100$ ('$\cdots$'), 200 ('- - -') and 502 ('—') depth levels ($\Delta z \approx 1$, 0.5 and 0.2 m): Lax-Wendroff (blue, reference), central (red) and first order upwind (green).

1.3.3 Impact of time discretization

The effect of time-discretization is investigated on Figure 4 where explicit, equally balanced explicit/implicit (Crank Nicholson, denoted as CN) and implicit schemes are compared for different sampling times t_s. The initial atmospheric scenarios being provided with t_s = 1 month, linear interpolation is used for a finer time resolution. The convection space discretization is achieved with a LW scheme. Concerning the implicit or explicit/implicit schemes, it appears that choosing t_s larger than a week tends to smooth out the transients due to seasonal variations (observed in the convective region for CO_2 and CH_4, and the peaks at 65-70 m for CH_3CCl_3 and $^{14}CO_2$). The explicit scheme necessitates a much smaller t_s and to keep $t_s/\Delta z$ below a specific constant (approximation of the Courant-Friedrichs-Lewy condition), hence significantly increasing the forward model simulation time, as reported in Table 2. Explicit discretization experiences the same sensitivity with respect to N as implicit discretization and an implicit scheme with $t_s = 1$ week provides the same results as an explicit scheme with $t_s = 30$ minutes. These results imply that an implicit or CN scheme with $t_s = 1$ week is the most suitable for the inverse diffusivity model at Greenland sites, as it provides a reasonable trade-off between accuracy and simulation time. Running this time-discretization test on Antarctic sites (not presented here) leads to the same conclusions. Finally, generating the Green's function and running the inverse scenario model for both implicit and CN schemes has shown that CN may induce numerical instabilities for the atmospheric history reconstruction. Implicit time discretization is thus retained as the final choice.

Overall, using appropriate depth and time steps, the sensitivity of our model to the tested dicretization schemes is much lower than its sensitivity to the number of gases used for diffusivity minimization (see next section). Similar differences in discretization schemes are unlikely to explain the differences between firn models used in the inter-comparison study of Buizert et al. (2012).

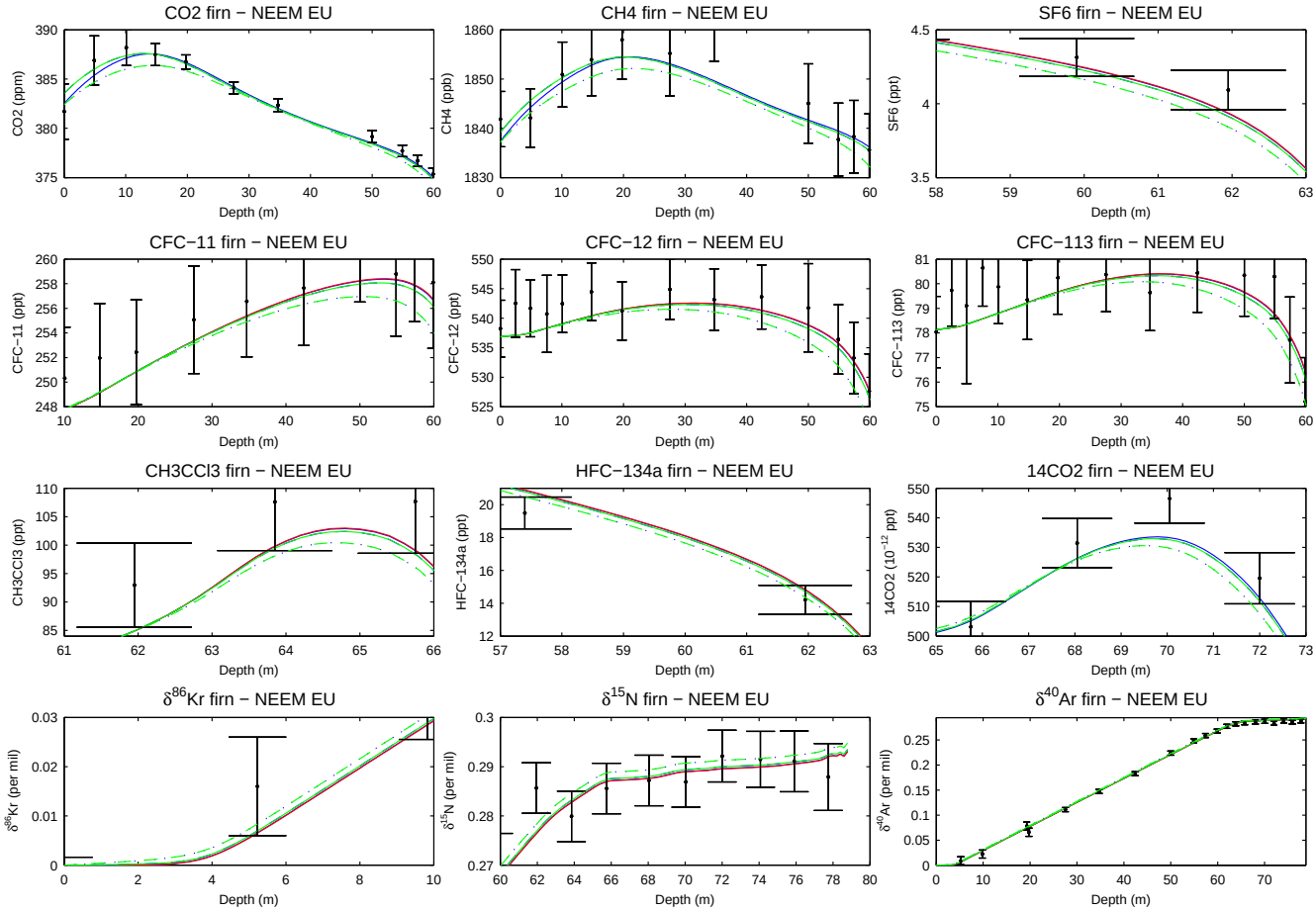

Fig. 4. Impact of time discretization on the trace gas mixing ratios at NEEM (EU hole, $\Delta z = 0.2$ m and a zoom on specific regions to highlight the differences): explicit with a sampling time t_s=15 minutes (red), implicit (blue) with $t_s = 1$ day ('—'), 1 week ('– – –') and 1 month ('- - -'), and implicit-explicit (green) with $t_s = 1$ week ('—') and 1 month ('– – –').

Table 2. Average simulation time per gas associated with the proposed time-discretization schemes for NEEM EU (1800 to 2008, full close-off depth at 78.8 m, 12 gases, left) and South Pole 1995 (1500 to 1995, full close-off depth at 123 m), obtained on a PC laptop equipped with the processor i5 540 m (2.53 Ghz, 3 Mo):

Method	t_s	Δz [a]	**Simulation time** [a]
Implicit	1 day	0.2 m	4.02 / 22.25 s
Implicit	1 week	0.2 m	0.63 / 3.91 s
Implicit	1 month	0.2 m	0.26 / 1.48 s
Explicit	15 min	0.2 m	5.09 / 29.45 min
Explicit	30 min	0.4 / 0.61 m	24.39 s / 1.34 min
Explicit	1 h	0.8 / 1.23 m	7.19 s / 12.13 s
Imp-explicit [b]	1 week	0.2 m	0.63 s / 3.77 s
Imp-explicit [b]	1 month	0.2 m	0.27 s / 1.48 s

[a]: NEEM EU / South Pole; [b]: Crank-Nicholson.

2 Inverse diffusivity model

2.1 Single versus multiple gases at NEEM US

Figures 5 and 6 are the NEEM-US equivalent of the NEEM-EU results presented in Section 3.4 of the article. Only three reference gas datasets are available for the NEEM-US drill hole whereas nine were measured for the NEEM-EU drill hole. Figures 5 and 6 illustrate the fact that using two reference gases already strongly improves the robustness of the calculated diffusivity with respect to using only one reference gas.

2.2 Additional sensitivity tests for NEEM-EU

The inverse model for diffusivity calculation requires an initial solution to start the minimization procedure. In order to evaluate the impact of this initial diffusivity distribution

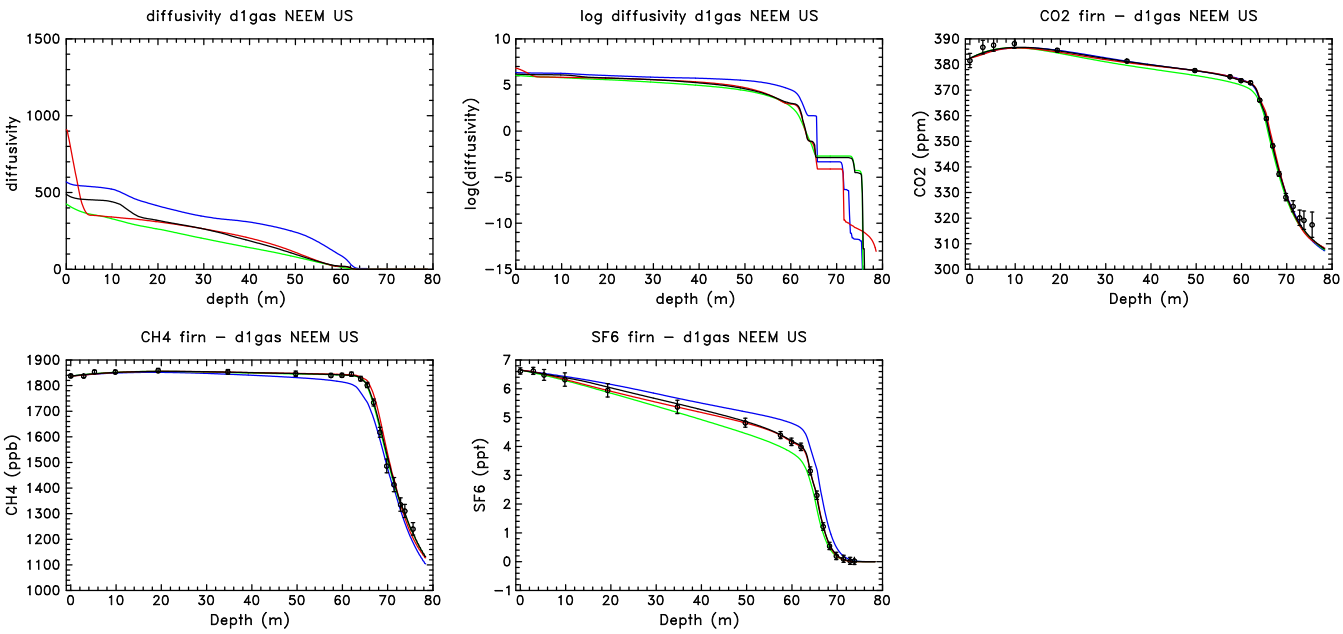

Fig. 5. Single gas inverse diffusivity model results for NEEM (US hole): each gas is used in turn to compute the diffusivity (reduced to CO_2, in m^2/year). Results are shown for CO_2 (blue), CH_4 (green) and SF_6 (red), and the 3 available gases (black, reference simulation).

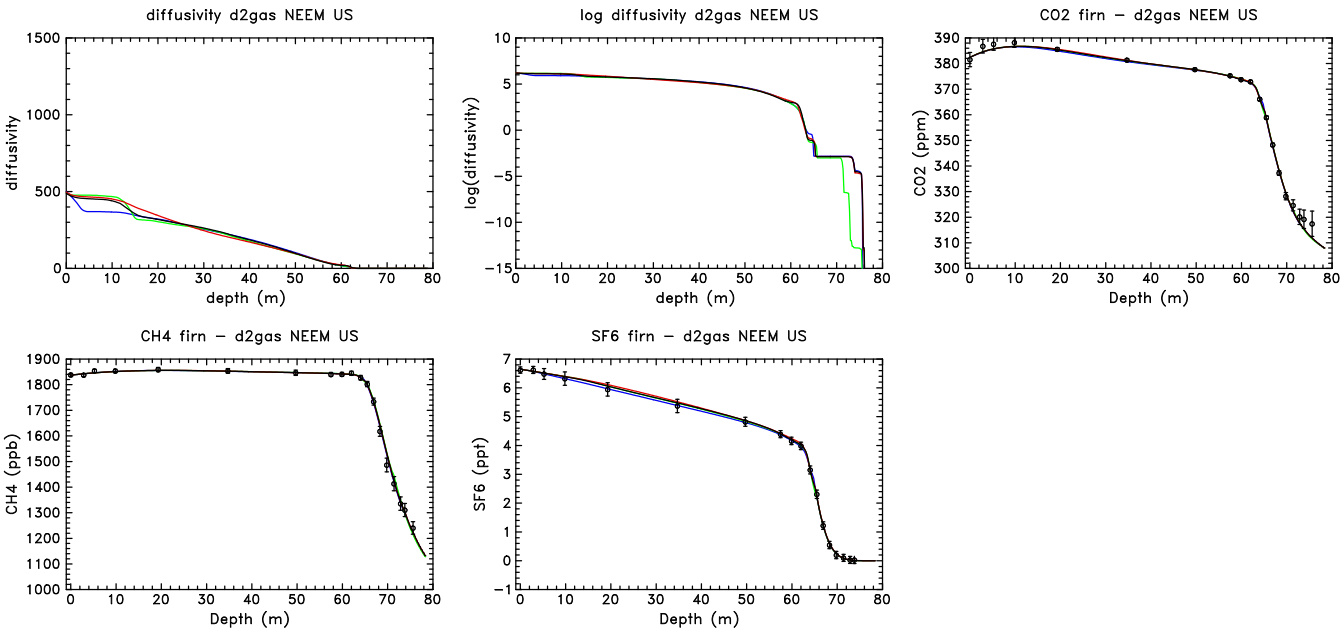

Fig. 6. Multiple gases inverse diffusivity model results for NEEM (US hole) using 2 reference gases: the dispersion of the diffusivities (reduced to CO_2, in m^2/year) and mixing ratios is greatly reduced in comparison with the single gas diffusivity depicted in Figure 5. Results are shown without CO_2 (blue), CH_4 (green) and SF_6 (red), and with the 3 available gases (black, reference simulation).

on our results, two different calculations were performed at each site:

- one using a rough parameterization of diffusivity versus open porosity;
- one using a null diffusivity at all depths.

The simple parameterization used in the first case is the following: if $f > 0.12$ and $D > 1$, $D = (2.6f - 0.312) * D_{\mathrm{air}}$, where D is the calculated initial diffusivity, f the depth-

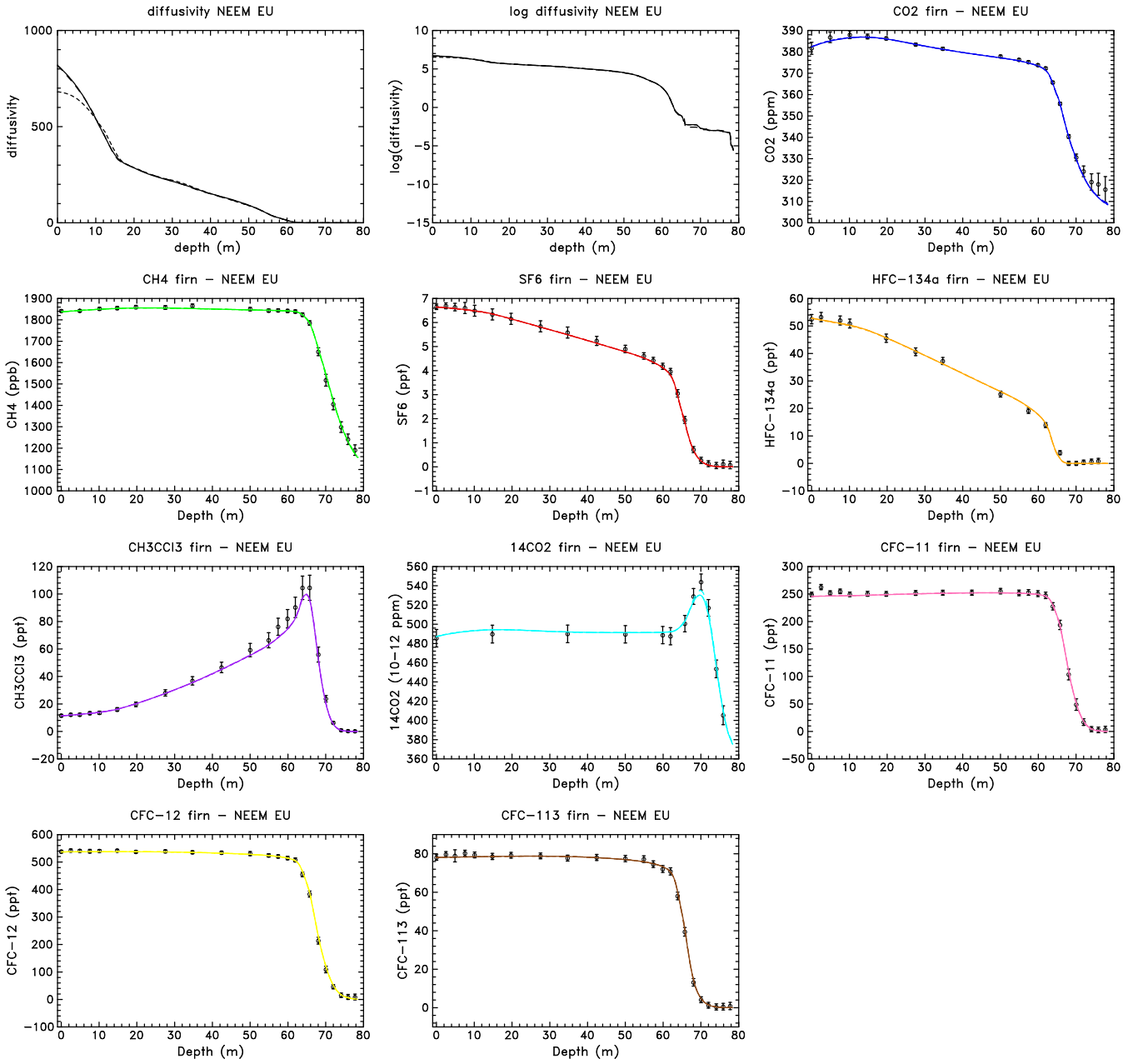

Fig. 7. Impacts of the initial solution and accumulation rate value at NEEM (EU hole) on the diffusivity profile (reduced to CO_2, in m^2/year): reference solution (with a parameterized initial solution and an accumulation rate averaged over 200 years) ('—'), initial solution at zero for all depths ('- - -') and accumulation averaged over 20 years ('– – –').

dependent open porosity of the firn and D_{air} the CO_2 diffusion coefficient in free air. Deeper in firn, defining z_1 as the first depth at which $f < 0.12$ or $D < 1$, the following equation is used: $D = 10^{10(z_1 - z)/(z_{\mathrm{F}} - z_1)}$, where z_{F} is the full bubble close-off depth ($f = 0$). The second formulation allows for a faster decrease of the diffusivity with depth than the first. Figure 7 shows that the initial diffusivity profile affects the final solution, but these differences are not large enough to induce a visible change on trace-gas mixing ratios in firn. As the minimization algorithm could converge to a local minimum (induced by the problem nonlinearities and non-uniqueness of the solution), the above two initial conditions were used at all modeled sites (see Section 3). Two similar solutions are always obtained, suggesting that the solutions are not importantly affected by local minima.

Likely in relation with Arctic warming, the snow accumulation rate at NEEM has varied in the recent past: the mean accumulation rate over the last 200 years (used in our

reference simulation) is 0.216 m/yr ice equivalent, whereas the best estimate current day accumulation is 0.227 m/yr ice equivalent (Buizert et al., 2012). Snow accumulation rate directly affects the firn sinking velocity (or advection), thus it can potentially influence the model results, especially in the bubble close-off zone. Our results show that the accumulation rate only affects the $^{14}CO_2$ peak (see Figure 7), which occurs deep in the air trapping region (in comparison with the location of the CH_3CCl_3 peak, the air trapping is multiplied by 2.6 and the open porosity by 0.8). This illustrates a limitation induced by the stationary hypothesis made on the firn sinking (induced by a constant accumulation rate) and the potential sensitivity of gases that have an important transient behavior in the close-off region.

Another source of uncertainty on the model results in deep firn is the chosen parameterization of the closed porosity versus depth. Using the parameterization proposed by Severinghaus and Battle (2006) (modified to match the full close-off depth of the reference simulation at NEEM) leads to a very similar result as modifying the accumulation rate: only the $^{14}CO_2$ peak height is affected, and it is similarly amplified. Using the parameterization proposed by Schwander (1989) induces no visible change from the reference solution (which uses Goujon et al., 2003). In a last test, the full close-off depth was shifted deeper by one meter. Once again, only the $^{14}CO_2$ peak height is affected, and it changes less than when modifying the accumulation rate. Finally we should note that the fit of the reference gases dataset is not significantly affected by these tests (the RMSD changes by less than 0.01).

3 Diffusivities at Arctic and Antarctic Sites other than NEEM

3.1 Datasets used to constrain the inverse model

For each reference gas, the model uses an atmospheric time trend and mixing ratios in firn together with the associated uncertainties. The methodology used here is very similar to the one described in detail by Buizert et al. (2012), thus this section will focus on the differences with respect to Buizert et al. (2012).

The base atmospheric time trend scenarios used for Arctic sites are those described in Buizert et al. (2012), and the Antarctic scenarios are their analogs built using the consistent (same data sources) South Hemisphere datasets. We should note that the short term variability (sub-monthly) of trace gas mixing ratios is smaller in the South Hemisphere than in the North Hemisphere as all species have dominant North Hemisphere emissions. Moreover, South Hemisphere ice core records were used when building North Hemisphere CO_2 and CH_4 scenarios, and the uncertainty on inter-hemispheric gradients does not apply to the South Hemisphere scenarios. Even with these reduced uncertainties, scenario errors are still the dominant error term in many cases for Antarctic sites. The calibration scales used to calculate best estimate trace gas mixing ratios have changed over time (see e.g. http://www.esrl.noaa.gov/gmd/ccl/summary_table.html). Moreover, scale differences between atmospheric measurement networks need to be taken into account (see Buizert et al., 2012, supplementary material). Our base atmospheric time trend scenarios were rescaled on a site by site basis to the most appropriate scale, taking into account relevant uncertainties. For instance, CH_3CCl_3 uncertainties include unexplained variable differences between AGAGE and NOAA network measurements (Buizert et al., 2012). The figures below thus display the original datasets together with model results using calibration scale-converted atmospheric time trend scenarios.

Uncertainties on firn data were estimated based on analytical precision and the consistency of duplicate measurements as in Buizert et al. (2012). When only few duplicates per drill site were measured, but datasets obtained with the same methodology were available at several sites, the mean uncertainty is calculated with the consistent pool of datasets. Buizert et al. (2012) considered seven sources of error in the overall uncertainty: (1) Analytical precision, (2) Uncertainty in atmospheric reconstructions, (3) Contamination with modern air in the deepest firn samples, (4) Inter-laboratory and inter-borehole offsets, (5) Possibility of in-situ CO_2 artifacts in deep firn, (6) Undersampling of seasonal cycle, (7) Unexplained EU-US borehole difference (SF_6 only). Errors (1), (2) and (6) were calculated with the same methodology. Error (4) could not be estimated in many cases as measurements were performed by a single laboratory. Error bars were enlarged when calibration-scale related issues were suspected, due to e.g. a constant offset in the upper firn between the forward model (scenario-based) results and firn data (see e.g. Martinerie et al., 2009). This reduces the weight of the suspect species with respect to other gases in the diffusivity calculation. Other error sources are site and species specific, we generally used data elimination rather than error bar enlarging in the presence of possibly contaminated data. Due to the fast diffusion of gases in the upper firn and age mixing in deep firn, trace gas profiles have to be somewhat smooth. Thus data points showing deviations from the expected smoothness are interpreted as outlier points. Eliminated data points are shown in grey on the following figures. In some cases (e.g. near the deepest sampling level), anomalous mixing ratios are not straightforwardly detected. Specific tests related to that issue were performed at some sites. We should note that site by site adaptation by increase of error bars or data elimination reduces the risk of producing a biased solution due to the strong weight attributed to anomalous data in the cost function. As a drawback, it also reduces the significance of comparing cost function values between sites. On the other hand, multi-gas diffusivity tuning can provide an improved way of evaluating the consistency of an overall dataset and detect outlier points.

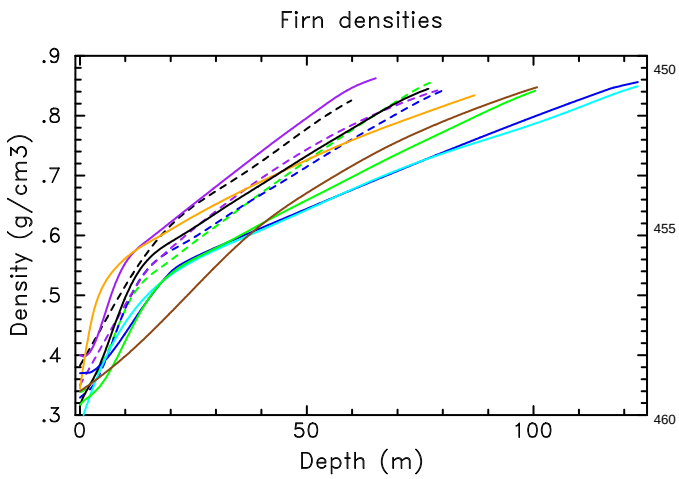

Fig. 8. Firn density versus depth for the sites considered. Arctic sites are shown with dashed lines: Devon Island in black, Summit in blue, NEEM in purple North GRIP in green. Antarctic sites are shown as continuous lines: DE08 in orange, Berkner in purple, Siple in yellow, South Pole 1995 in dark blue, South Pole 2001 in light blue, Dronning Maud Land in black, Dome C in green and Vostok in brown.

Another important model constraint is the firn density profile. The density profiles used here are shown on Fig. 8. All our density profiles are based on experimental data (obtained by weighting and measuring the firn core). We use smooth mathematical functions fitted to the density data such as in e.g. Buizert et al. (2012); Severinghaus and Battle (2006) in order to obtain a regular and monotonous density profile. It should be noted that numerous calculations in firn model use first and/or second derivatives of the density, thus precise density profiles are desirable especially in the deep firn, where density gradients are small. An important limit to the precision of density measurements is the firn core volume estimation, which can be biased by the irregular shape of the core. Precision can be gained by polishing the firn core with a lathe, but to our knowledge this was not performed at most sites.

A surface density dependent parameter is used in the convective zone diffusivity calculation, c_f: the surface value of the open porosity. Ideally, a site dependent value of c_f should be used, but near surface density measurements require specific methods and generally the near-surface values of our density profiles are extrapolated from measurements performed deeper in the snow. Thus a constant value of c_f = 0.65 is used for all sites. Further site by site indications are provided in the relevant sections below.

3.2 DE08

DE08 is located near the summit of the Antarctic Law Dome. The measurements shown on Figure 9 were sampled at DE08-2 and performed at CSIRO (see Trudinger et al., 1997, and references therein). The deepest CFC-11 sample is inconsistent with the overall dataset and considered as an outlier (not used in diffusivity calculation). A more ambiguous situation occurs for the deepest CO_2 sample for which the model/data difference falls just outside the error bar. As DE08 is a warm site, a deep firn CO_2 anomaly similar to the one observed at NEEM (Buizert et al., 2012) or North GRIP (see Section 3.5) could be suspected. A sensitivity test was performed to compare diffusivities calculated with/without this data point. The effect is limited to the deepest firn, and CH_4 (a fast diffusing species) is the most affected.

3.3 Devon Island

Devon Island, North GRIP, Berkner Island, Dronning Maud Land and Dome C firn air pumping operations were performed in the frame of two EC research programs, most datasets for these sites are available from the BADC database (FIRETRACC, 2007; CRYOSTAT, 2007). In this study, we used LGGE data for CO_2 and CH_4, and UEA halocarbon data to maximize the consistency of our diffusivities in the perspective of multi-site atmospheric time-trend reconstructions.

Multi-gas constrained diffusivity (Fig. 10) brings a remarkable improvement to the fit of the Devon Island dataset with respect to single-gas diffusivity (Martinerie et al., 2009). Only the multi-gas diffusivity follows the unusual wiggles in the trace gas depth-mixing ratio profiles, which are likely due to the presence of about 150 refrozen melt layers in the Devon Island firn.

3.4 Summit

Reference gas measurements for Summit 2006 were performed at NOAA ESRL. A specific issue for this site is the inconsistency of the SF_6 dataset with the other trace-gas data (see Figure 11). At the time of Summit 2006 firn air measurement, the NOAA ESRL analytical system was optimized to measure near ambient SF_6 values, and a calibration bias is suspected for lower SF_6 mixing ratios. Buizert et al. (2012) also describes SF_6 specific issues at NEEM. We should note that NEEM and Summit are the most recently drilled sites in this study (2008 and 2006), thus an inconsistency of the firn data with the recent SF_6 scenario could also contribute to the SF_6 upper firn issues at NEEM and Summit. Summit diffusivities were calculated with/without SF_6. The most affected species are those with the latest emission start: CFC-113 and HFC-134a. As including SF_6 brings the fit of CFC-113 and HFC-134a outside error bars at some depths without allowing for a good fit of SF_6, the diffusivity calculated without SF_6 is used as our reference diffusivity.

The sensitivity test on the influence of the full close-off depth (z_F) performed for NEEM was replicated at Summit using a larger change in z_F (z_F = 84 m instead of z_F = 80.8 m). Only slight changes of the diffusivity were obtained,

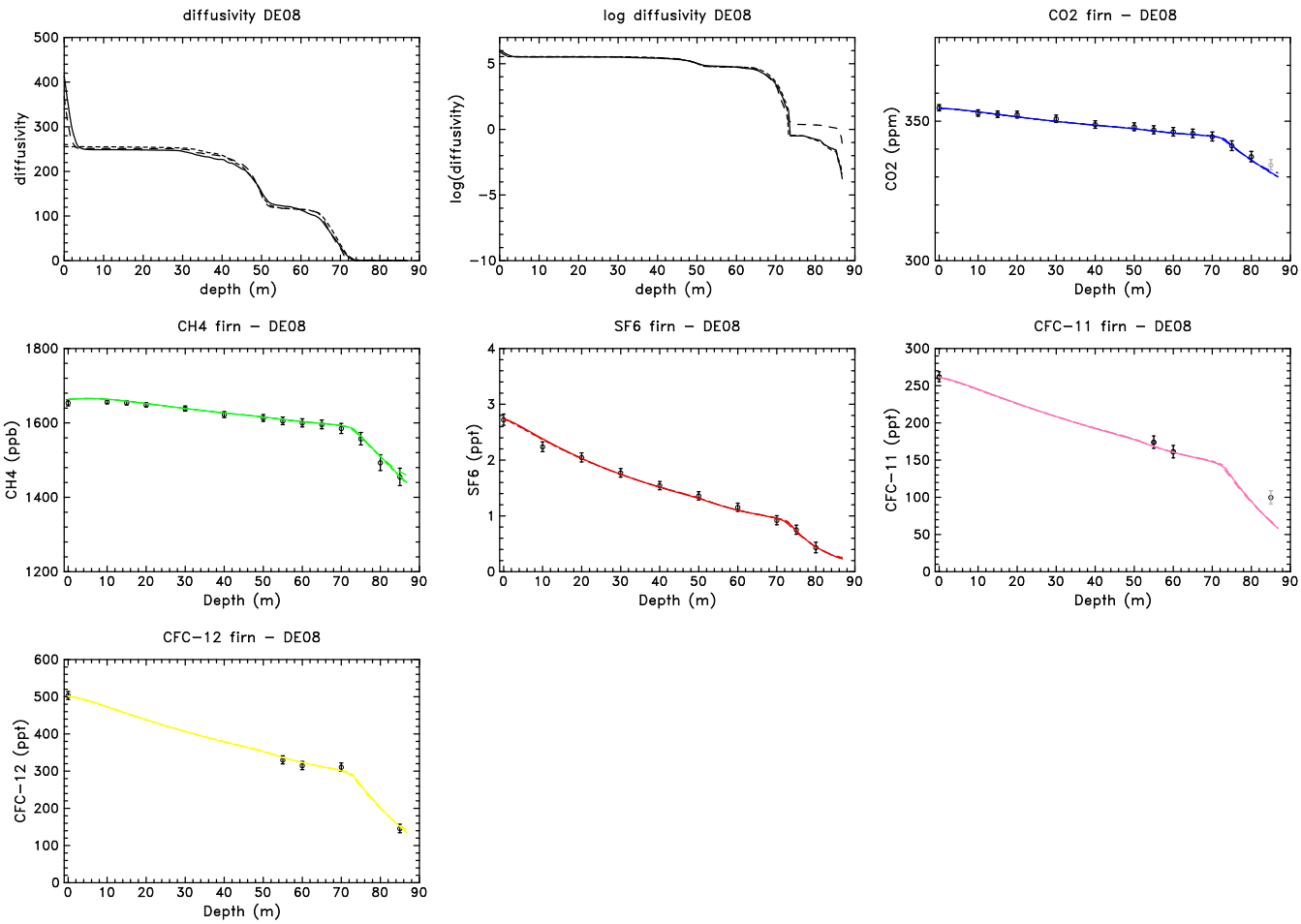

Fig. 9. Diffusivity (reduced to CO_2, in m^2/year) and gas mixing ratios at DE08: parameterized initial diffusivity ('—'), zero initial diffusivity ('- - -') and using CO_2 at the deepest level ('– – –').

and reference gases were unaffected except for a slight reduction of the CH_3CCl_3 peak (remaining within error bars).

3.5 North GRIP

North GRIP firn data were introduced in Section 3.3. We should note that the two deepest CO_2 data points show a similar anomaly as in the NEEM firn (Buizert et al., 2012). North GRIP presents a unique feature in the near-surface firn (Fig. 12): firn data in the first ∼8 meters deviate from the monthly scenarios for at least three species: SF_6, CFC-11 and CFC-12. This may be interpreted as the fast diffusion in the firn of an atmospheric anomaly. This situation looks like what is expected in a firn convective zone where very rapid transport would produce an absence of mixing ratio gradient with respect to the atmosphere. However, the modeled surface mixing ratios cannot deviate from the scenario values at drill date, and the diffusivity calculation produces very variable results in the upper 10 meters. Artificially setting the drill date atmospheric scenario values to the near-surface firn value for SF_6, CFC-11 and CFC-12 leads to a correct simulation of the upper firn results. Thus the suspected atmospheric event should have occurred at a sub-monthly time scale (our atmospheric scenarios have a monthly time step). Most importantly, deeper firn mixing ratios show very little sensitivity to the near-surface diffusivity.

3.6 Berkner

Berkner firn data were introduced in Section 3.3. A specific issue for this site is the fact that data below 58 m depth are suspected to be contaminated by a leak in the air pumping system (Worton et al., 2007). Using no data below 57 m depth (Fig. 13) produces a good match of the non-suspect dataset but leads to anomalously narrow age distributions by comparison with other sites. Using the apparently least contaminated data point: CH_4 at 63 m depth leads to Green functions more consistent with other sites without modifying the fit of the other data. The absence of constraint in the deep Berkner firn thus likely leads to an increased uncertainty on

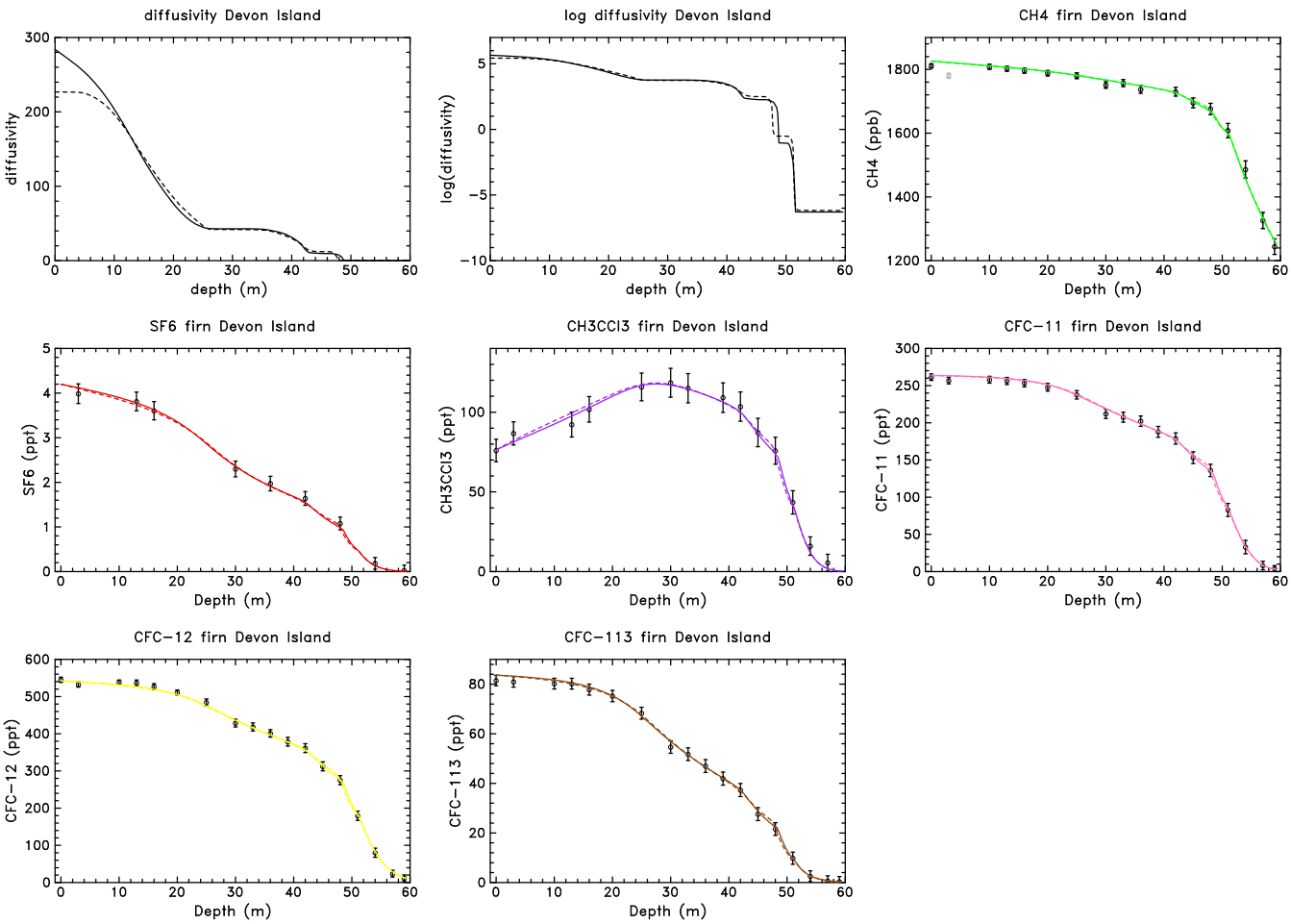

Fig. 10. Diffusivity (reduced to CO_2, in m^2/year) and gas mixing ratios at Devon Island: parameterized initial diffusivity ('—') and zero initial diffusivity ('- - -').

the Green function.

3.7 Siple Dome

Reference gas measurements for Siple Dome were performed at NOAA ESRL (Butler et al., 1999). At 55 m depth, all species show a positive mixing ratio anomaly (see Figure 14), thus this depth level was not taken into account in diffusivity calculation. A specific test was performed for the 56.5 m depth level: halocarbon measurements at very low mixing ratio levels are difficult to perform and can be more sensitive to contamination. In our base case simulations, only the CO_2 mixing ratio is considered at this last measurement depth. If mixing ratios of SF_6, CFC-11, CFC-113 and CH_3CCl_3 at 56.5 m depth are also taken into account, the modeled CO_2 mixing ratio increases, deviating from the CO_2 deepest data point.

3.8 South Pole

Two drilling operations performed at South Pole in 1995 (Fig. 15) and 2001 (Fig. 16) were modeled. Reference gas measurements for South Pole were performed at NOAA ESRL (Battle et al., 1996; Butler et al., 1999).

Halocarbon mixing ratios in the deep South Pole 1995 firn show non-monotonous variations. Data points below the shallowest level showing a higher mixing ratio than the upper depth level were not considered for diffusivity calculation (except for SF_6, for which it would have eliminated all data below 70 m).

Less reference gas data are available for South Pole 2001. Sampling procedure tests were performed during this drilling operation, which may explain the presence of outlier points also for CO_2 and CH_4. A forward model test was performed using the South Pole 1995 reference diffusivity while simulating South Pole 2001. The fit of the reference gas data exceeds error bars only around 115 m depth. We should note that our simulation conditions are more different between

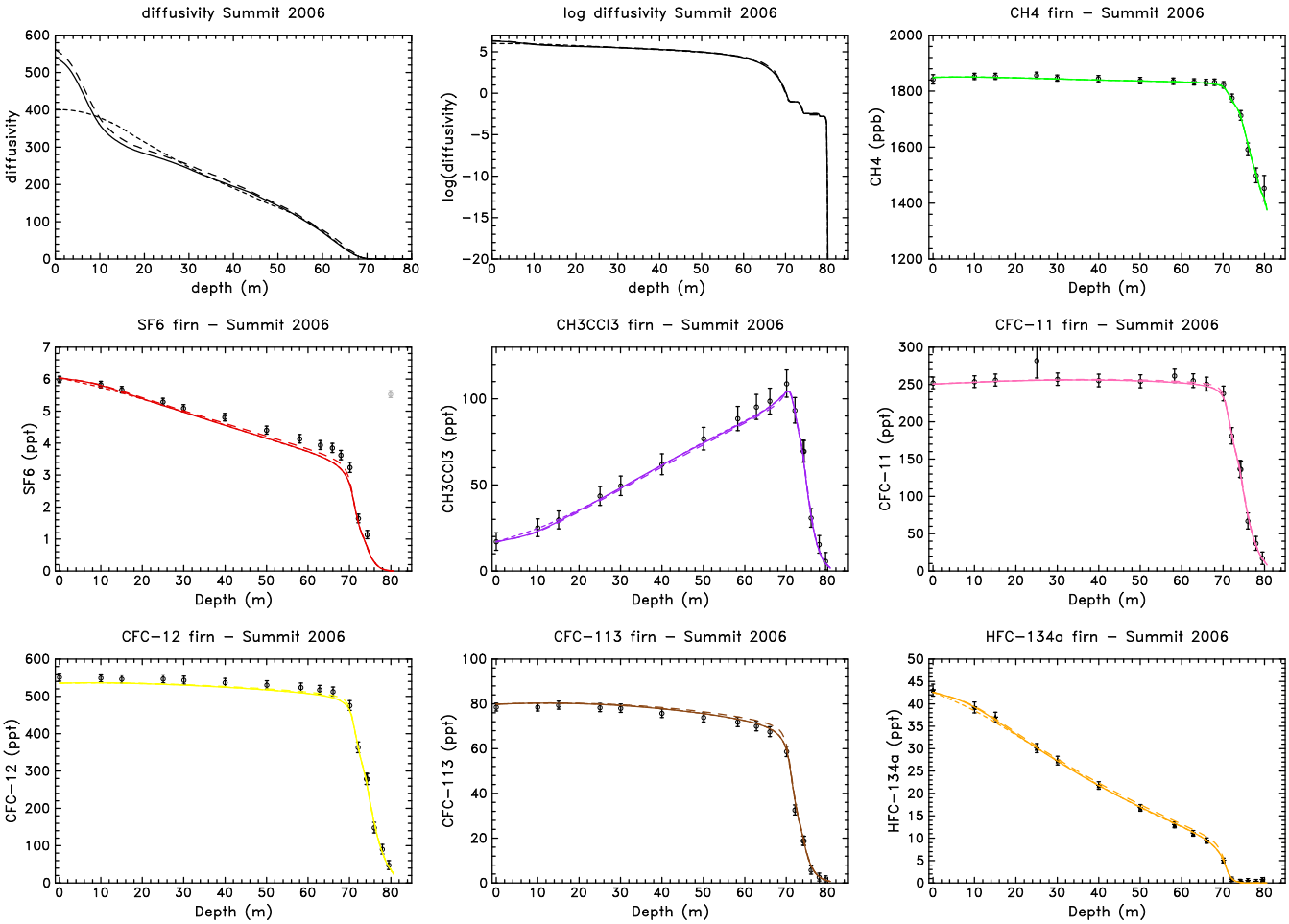

Fig. 11. Diffusivity (reduced to CO_2, in m^2/year) and gas mixing ratios at Summit: parameterized initial diffusivity ('—'), zero initial diffusivity ('- - -') and using SF_6 as a reference gas ('– – –').

South Pole 1995 and South Pole 2001 than between NEEM-EU and NEEM-US. In addition to the use of different end dates (drill dates) for the atmospheric scenarios, the South Pole simulations use different density profiles (measured for each operation).

3.9 Dronning Maud Land

Dronning Maud Land (DML) firn data were introduced in Section 3.3. The CH_4 (and to a lesser extent CO_2) data at this site show unusual wiggles (Fig 17). As a consequence an increased experimental uncertainty (15 ppb instead of 10 ppb) was assigned to CH_4 at DML. The initial solution test provides somewhat different solutions in the upper firn, although within error bars. One produces a better fit of CH_3CCl_3, and a degraded fit of SF_6, the other one does the reverse. The two fits are of nearly equivalent quality (their root mean square deviations from the data (RMSD) differ by less than 1%). Thus the DML case illustrates the fact that our inverse algorithm does not always find the absolute minimal solution. However the numerous tests performed at 13 drill sites never produced a seemingly erratic behavior of the model, or solutions with significantly different quality.

3.10 Dome C

Dome C firn data were introduced in Section 3.3. Dome C is the site where the RMSD minimized by the inversion algorithm is the highest ($RMSD = 0.98$). The model/data comparison on Figure 18 suggests that the model has difficulty to reconcile the different datasets around 85-90 meters depth. Near surface unfitted points (CO_2 at ~ 0 m and ~ 10 m, CFC-12 at ~ 0 m), which might be due to the inability of the model to capture sub-monthly time scale atmospheric variability, have a high weight in the cost function and also degrade the quality indicators of the solution.

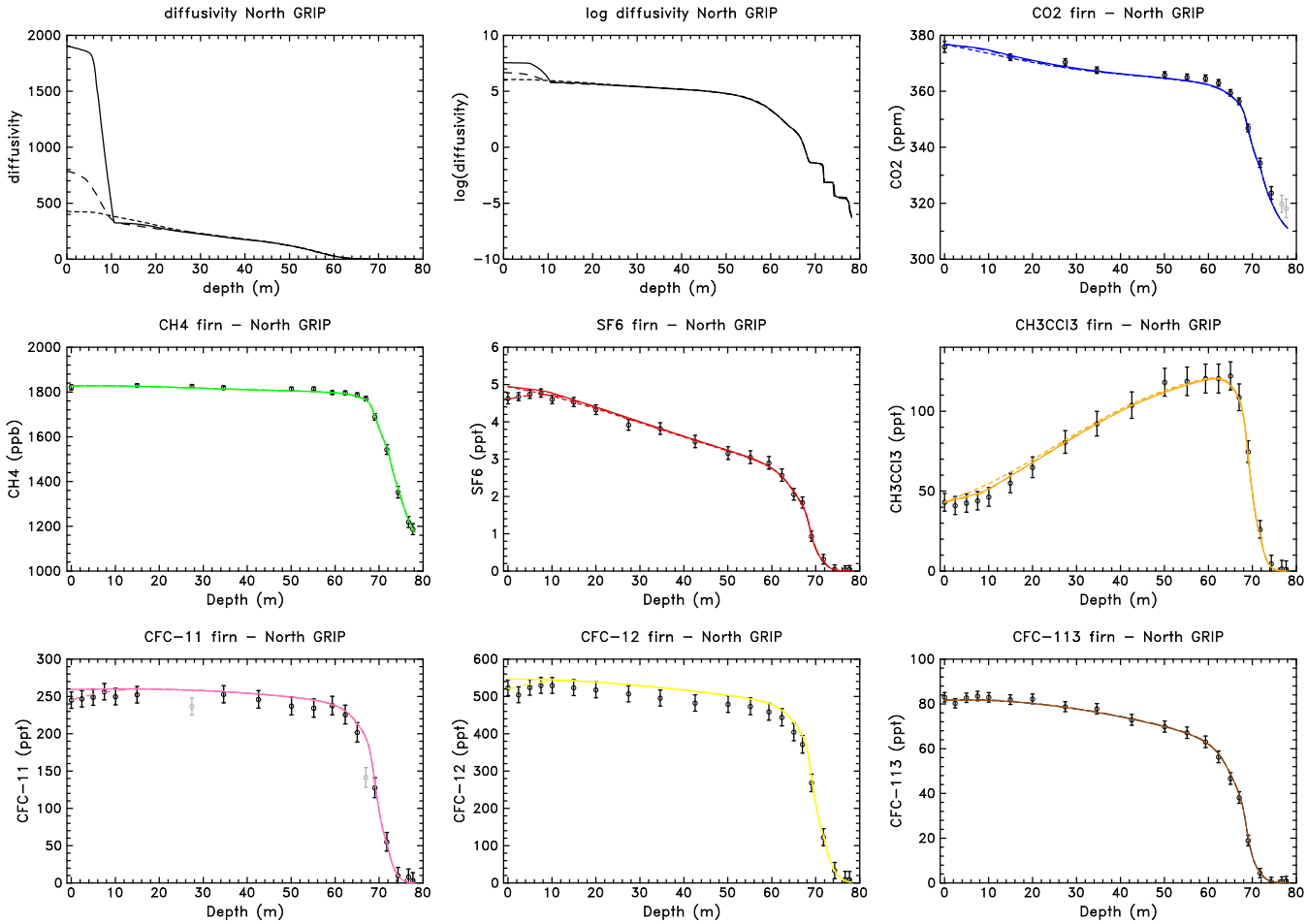

Fig. 12. Diffusivity (reduced to CO_2, in m^2/year) and gas mixing ratios at North GRIP: parameterized initial diffusivity ('—'), zero initial diffusivity ('- - -') and changing the final (drill date) atmospheric scenario values for SF_6, CFC-11 and CFC-12 ('– – –').

3.11 Vostok

CO_2 and CH_4 measurements in the Vostok firn were performed at LGGE (Rommelaere et al., 1997). The two reference gases are very consistent: the model fits both datasets well within error bars (see Figure 19). The ^{15}N of N_2 record at Vostok shows a 13 m deep convective zone: gravitational fractionation of ^{15}N starts at 13 m depth (Bender et al., 1994). The model gravitational settling for all gases also starts at 13 m depth for the reference simulation and the initial solution test. In the second test shown in Figure 19, modeled gravitational settling starts at the firn surface. The upper firn diffusivity produced is less different from the reference case than the diffusivity from the null initial solution test. However in the initial solution test, higher diffusivities above 20 m seem compensated by lower diffusivities below and produce no visible difference on the modeled trace gas mixing ratios, and a RMSD close to the reference solution (3.5% difference). On the other hand, starting gravitational settling at the surface leads to a RMSD increase by 35%) and modifies somewhat the fit of the CO_2 dataset. In our inverse model context, this does not mean that CO_2 is more affected by gravitational settling than CH_4, but that the model prioritizes the fit of CH_4 data, which have smaller error bars (in fact a higher signal to noise ratio) in the upper firn.

4 Estimation of the diffusivity with a scaling law

The impact of estimating CO_2 diffusivity with our scaling law from Eqs. (20)-(21) in the main paper is illustrated on Figs. 20 and 21. The scaling captures reasonably well the upper firn diffusivity (Fig. 20) and upper firn CO_2 and CH_4 mixing ratios (Fig. 21) at most sites. The sigmoid approximation for the LIZ also provides fairly consistent profile estimates for the LID transition. Gas transport in deep firn tends to be overestimated at NEEM, Summit and Dronning Maud Land and underestimated at Vostok, but remains within acceptable bounds considering the simplicity of the scaling law. As expected, the largest misfit is obtained at Devon Island.

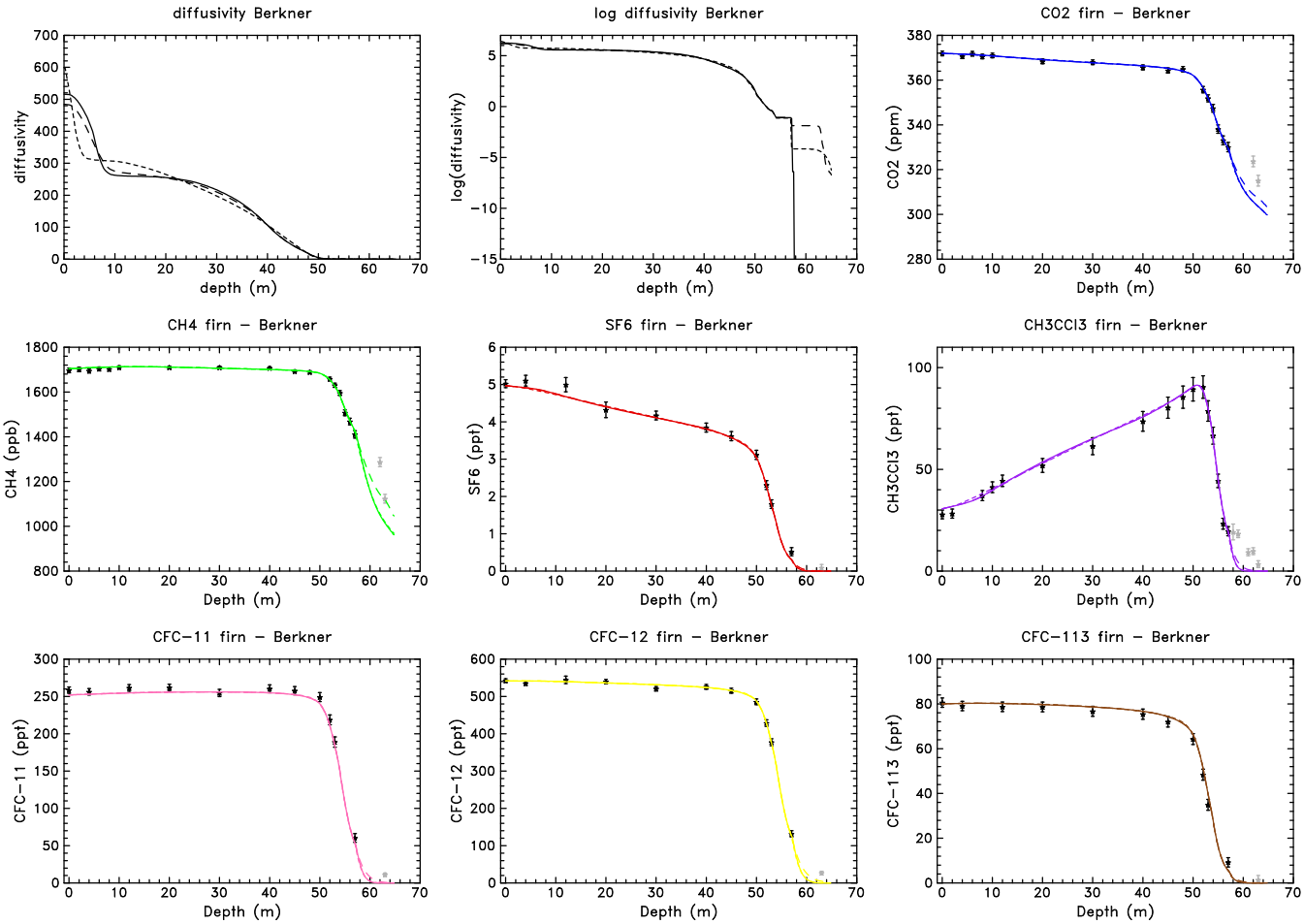

Fig. 13. Diffusivity (reduced to CO_2, in m^2/year) and gas mixing ratios at Berkner: parameterized initial diffusivity ('—'), zero initial diffusivity ('- - -') and using CH_4 in the last depth level ('– – –').

References

Battle, M., Bender, M., Sowers, T., Tans, P., Butler, J. H., Elkins, J. W., Ellis, J., Conway, T., Zhang, N., Lang, P., and Clarke, A.: Atmospheric gas concentrations over the past century measured in air from firn at the South Pole, Nature, 383, 231–235, 1996.

Bender, M. L., Sowers, T., Barnola, J.-M., and Chappellaz, J.: Changes in the O_2/N_2 ratio of the atmosphere during recent decades reflected in the composition of air in the firn at Vostok Station, Antarctica, Geophys. Res. Lett., 21, 189–192, 1994.

Buizert, C., Martinerie, P., Petrenko, V., Severinghaus, J., Trudinger, C., Witrant, E., Rosen, J., Orsi, A., Rubino, M., Etheridge, D., Steele, L., Hogan, C., Laube, J., Sturges, W., Levchenko, V., Smith, A., Levin, I., Conway, T., Dlugokencky, E., Lang1, P., Kawamura, K., Jenk, T., White, J., Sowers, T., Schwander, J., and Blunier, T.: Multiple-tracer firn air transport characterisation and model intercomparison for NEEM, Northern Greenland, Atmos. Chem. Phys., 12, 4259–4277, doi: 10.5194/acp-12-4259-2012, 2012.

Butler, J. H., Battle, M., Bender, M. L., Montzka, S. A., Clarke, A. D., Saltzman, E. S., Sucher, C. M., Severinghaus, J. P., and Elkins, J. W.: A record of atmospheric halocarbons during the twentieth century from polar firn air, Nature, 399, 749–755, 1999.

Coussy, O.: Poromechanics, John Wiley & Sons Ltd, 2nd edn., 2003.

CRYOSTAT: CRYOspheric STudies of Atmospheric Trends in stratospherically and radiatively important gases (CRYOSTAT), http://badc.nerc.ac.uk/data/cryostat, access: January 2011, 2007.

FIRETRACC: Firn Record of Trace Gases Relevant to Atmospheric Chemical Change over 100 yrs (FIRETRACC/100), http://badc.nerc.ac.uk/data/firetracc, access: January 2011, 2007.

Freitag, J., Dobrindt, U., and Kipfstuhl, J.: A new method for predicting transport properties of polar firn with respect to gases on the pore-space scale, Ann. Glaciol., 35, 538–544, 2002.

Goujon, C., Barnola, J.-M., and Ritz, C.: Modeling the densification of firn including heat diffusion: application to close-off, J. Geophys. Res., 108, ACL10.1–ACL10.18, doi:10.1029/2002JD003319, 2003.

Hirsch, C.: Numerical Computation of Internal and External Flows, vol. 1: The Fundamentals of Computational Fluid Dynamics, Butterworth-Heinemann, 2nd edn., 2007.

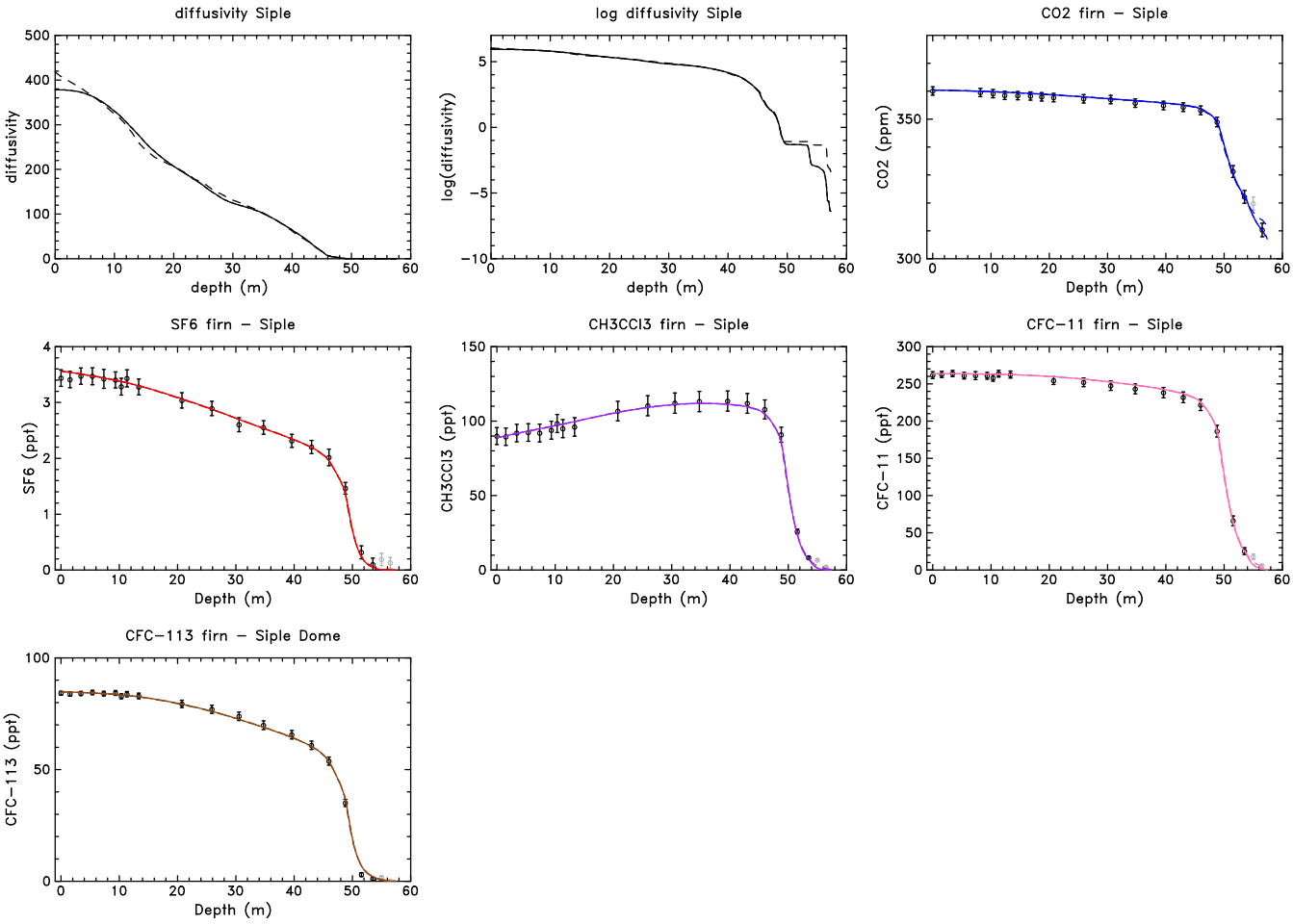

Fig. 14. Diffusivity (reduced to CO_2, in m^2/year) and gas mixing ratios at Siple Dome: parameterized initial diffusivity ('—'), zero initial diffusivity ('- - -') and with data points at 56.5m depth for SF6, CFC-11, CFC-113 and CH_3CCl_3 ('– – –').

Martinerie, P., Raynaud, D., Etheridge, D., Barnola, J., and Mazaudier, D.: Physical and climatic parameters which influence the air content in polar ice, Earth and Planetary Science Letters, 112, 1–13, 1992.

Martinerie, P., Lipenkov, V., Raynaud, D., Chappellaz, J., Barkov, N., and Lorius, C.: Air content paleo record in the Vostok ice core (Antarctica): a mixed record of climatic and glaciological parameters, J. Geophys. Res., 99, 10 565–10 576, 1994.

Martinerie, P., Nourtier-Mazauric, E., Barnola, J.-M., Sturges, W. T., Worton, D. R., Atlas, E., Gohar, L. K., Shine, K. P., and Brasseur, G. P.: Long-lived halocarbon trends and budgets from atmospheric chemistry modelling constrained with measurements in polar firn, Atmos. Chem. Phys., 9, 3911–3934, doi: 10.5194/acp-9-3911-2009, http://www.atmos-chem-phys.net/9/3911/2009/, 2009.

Mattheij, R., Rienstra, S., and ten Thije Boonkkamp, J.: Partial Differential Equations: Modeling, Analysis, Computation, Monographs on Mathematical Modeling and Computation, SIAM, Philadelphia, 2005.

Rommelaere, V., Arnaud, L., and Barnola, J.: Reconstructing recent atmospheric trace gas concentrations from polar firn and bubbly ice data by inverse methods, J. Geophys. Res., 102, 30 069–30 083, 1997.

Schwander, J.: The transformation of snow to ice and the occlusion of gases, in: The Environmental Record in Glaciers and Ice Sheets, edited by Oeschger, H. and Langway Jr., C., pp. 53–67, John Wiley, New York, 1989.

Severinghaus, J. and Battle, M.: Fractionation of gases in polar ice during bubble close-off: New constraints from firn air Ne, Kr and Xe observations, Earth Planet. Sci. Lett., pp. 474–500, 2006.

Severinghaus, J., Sowers, T., Brook, E., Alley, R., and Bender, M.: Timing of abrupt climate change at the end of the Younger Dryas period from thermally fractionated gases in polar ice, Nature, 391, 1998.

Severinghaus, J. P., Albert, M. R., Courville, Z. R., Fahnestock, M. A., Kawamura, K., Montzka, S. A., Mühle, J., Scambos, T. A., Shields, E., Shuman, C. A., Suwa, M., Tans, P., and Weiss, R. F.: Deep air convection in the firn at a zero-accumulation site, central Antarctica, Earth Planet. Sci. Lett., 293, 359–367, 2010.

Trudinger, C., Enting, L., Etheridge, D., Francey, R., Levchenko, V., Steele, L., Raynaud, D., and Arnaud, L.: Modeling air movement and bubble trapping in firn, J. Geophys. Res., 102, 6747–6763,

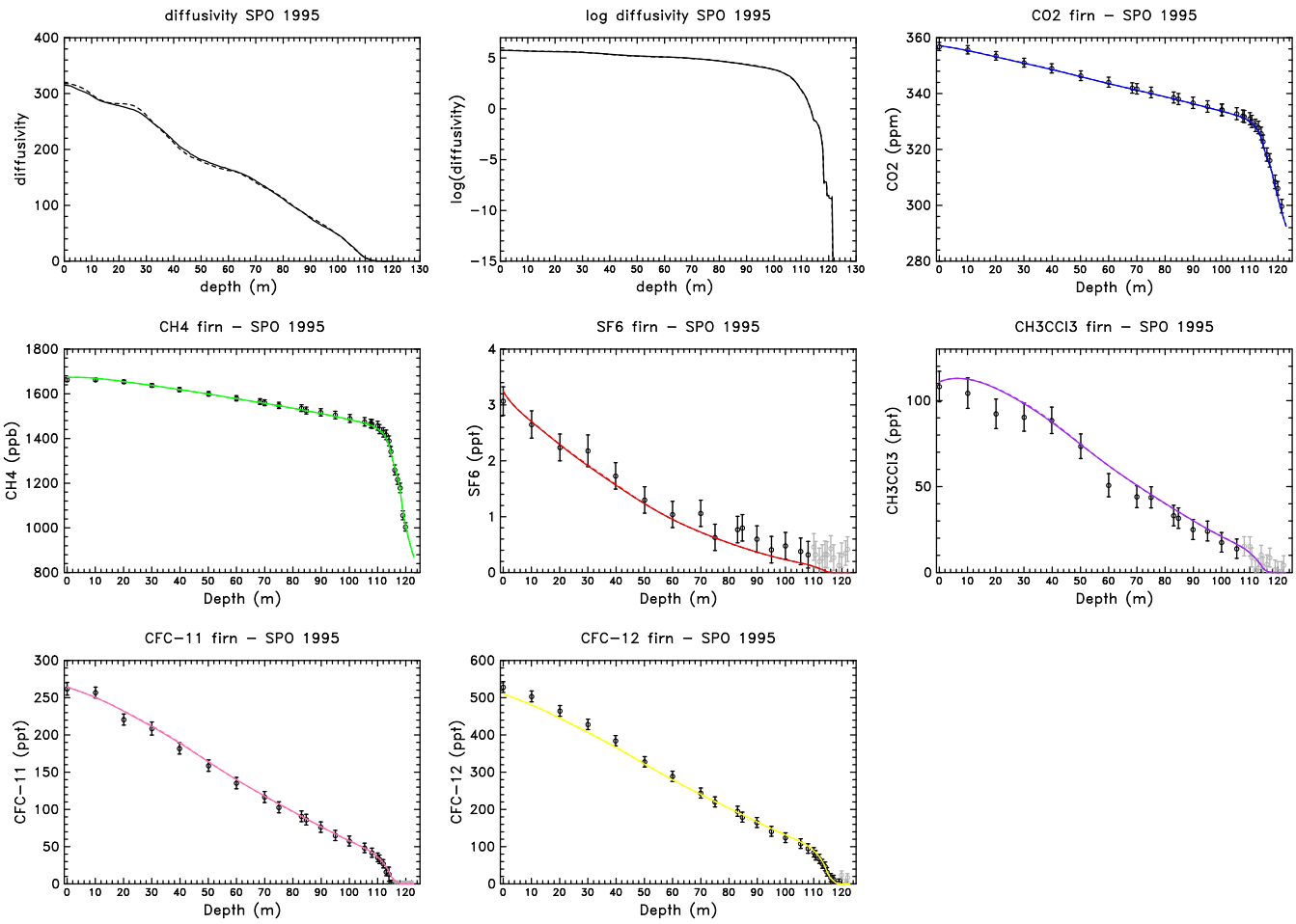

Fig. 15. Diffusivity (reduced to CO_2, in m^2/year) and gas mixing ratios at South Pole in 1995: parameterized initial diffusivity ('—') and zero initial diffusivity ('- - -').

1997.

Witrant, E. and Martinerie, P.: Input Estimation from Sparse Measurements in LPV Systems and Isotopic Ratios in Polar Firns, in: Proc. of the IFAC Joint Symposium on SSSC, TDS and FDA, Grenoble, France, 2013.

Worton, D. R., Sturges, W. T., Gohar, L. K., Shine, K. P., Martinerie, P., Oram, D. E., Humpfrey, S. P., Begley, P., Gunn, L., Barnola, J.-M., Schwander, J., and Mulvaney, R.: Atmospheric Trends and Radiative Forcings of CF_4 and C_2F_6 Inferred from Firn Air, Environ. Sci. Technol., 41, 2184–2189, 2007.

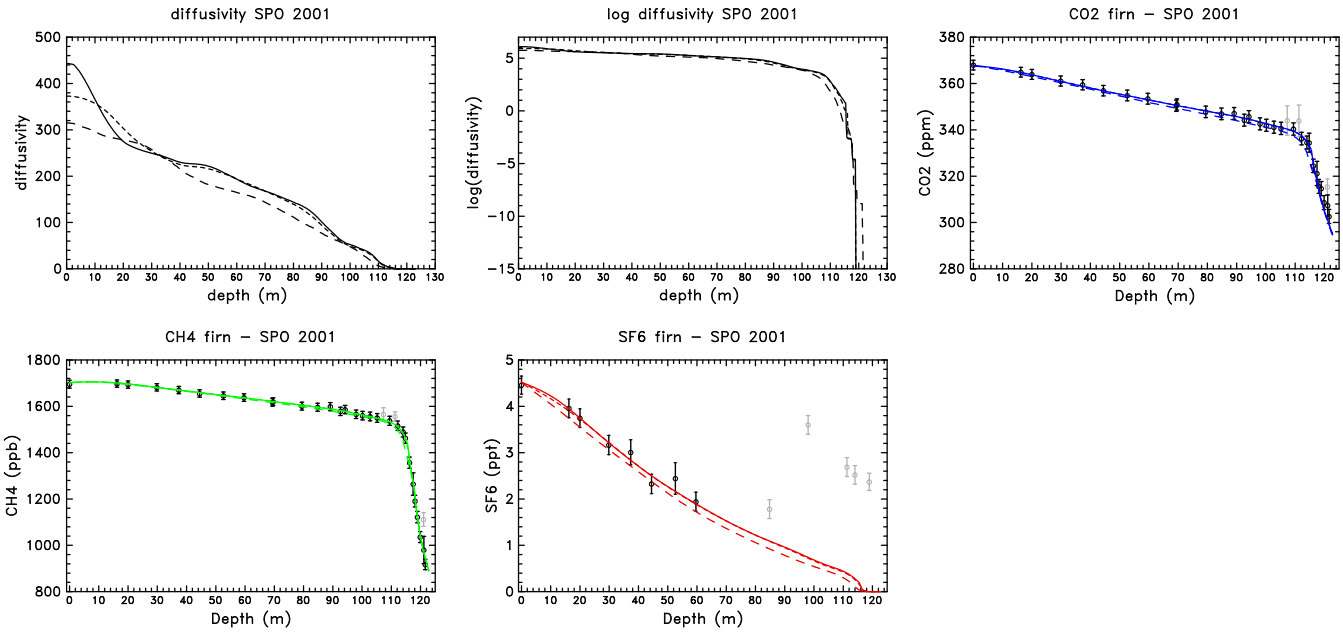

Fig. 16. Diffusivity (reduced to CO_2, in m^2/year) and gas mixing ratios at South Pole in 2001: parameterized initial diffusivity ('—'), zero initial diffusivity ('- - -') and with the diffusivity obtained from the 1995 measurements ('– – –').

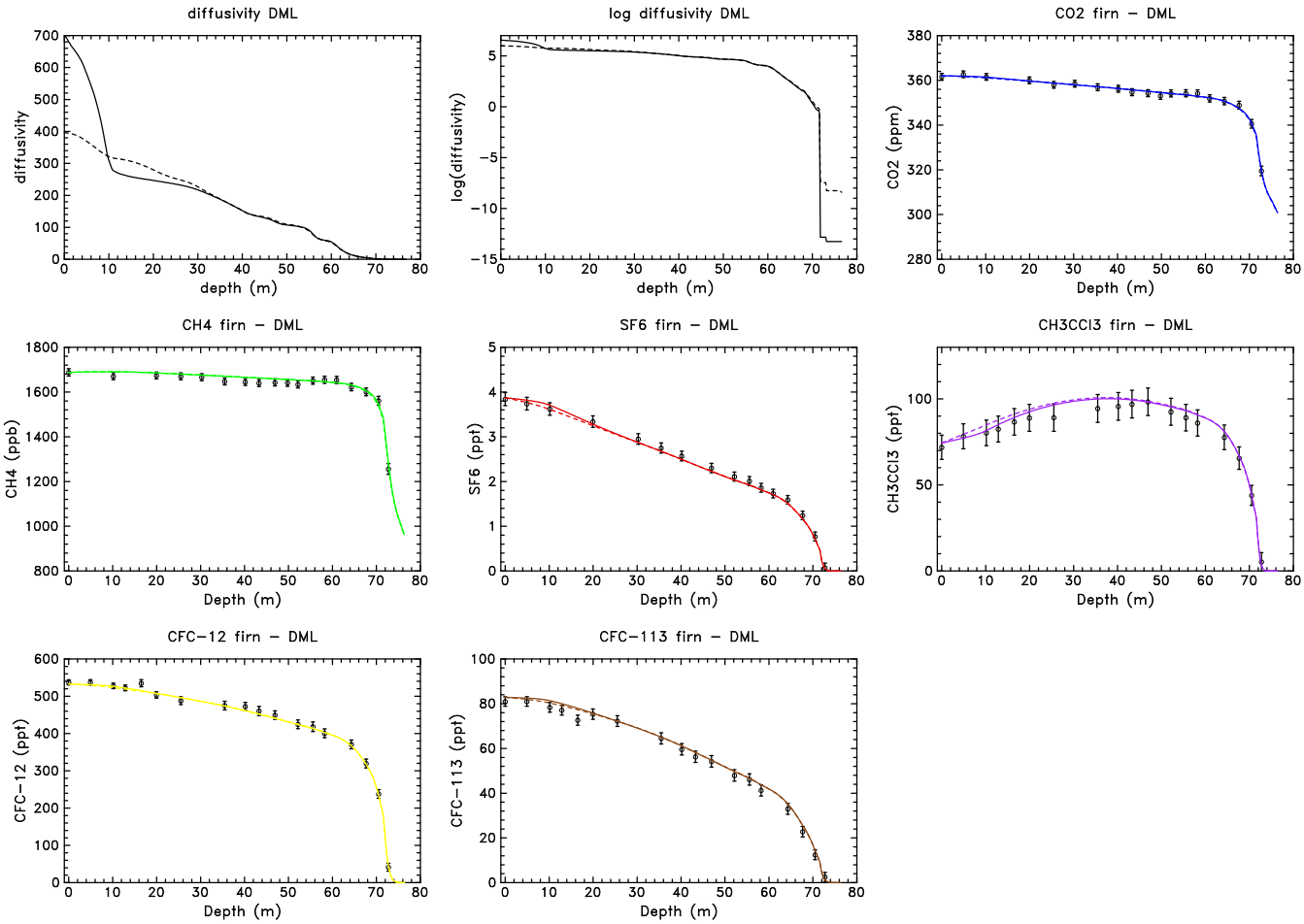

Fig. 17. Diffusivity (reduced to CO_2, in m^2/year) and gas mixing ratios at DML: parameterized initial diffusivity ('—') and zero initial diffusivity ('- - -').

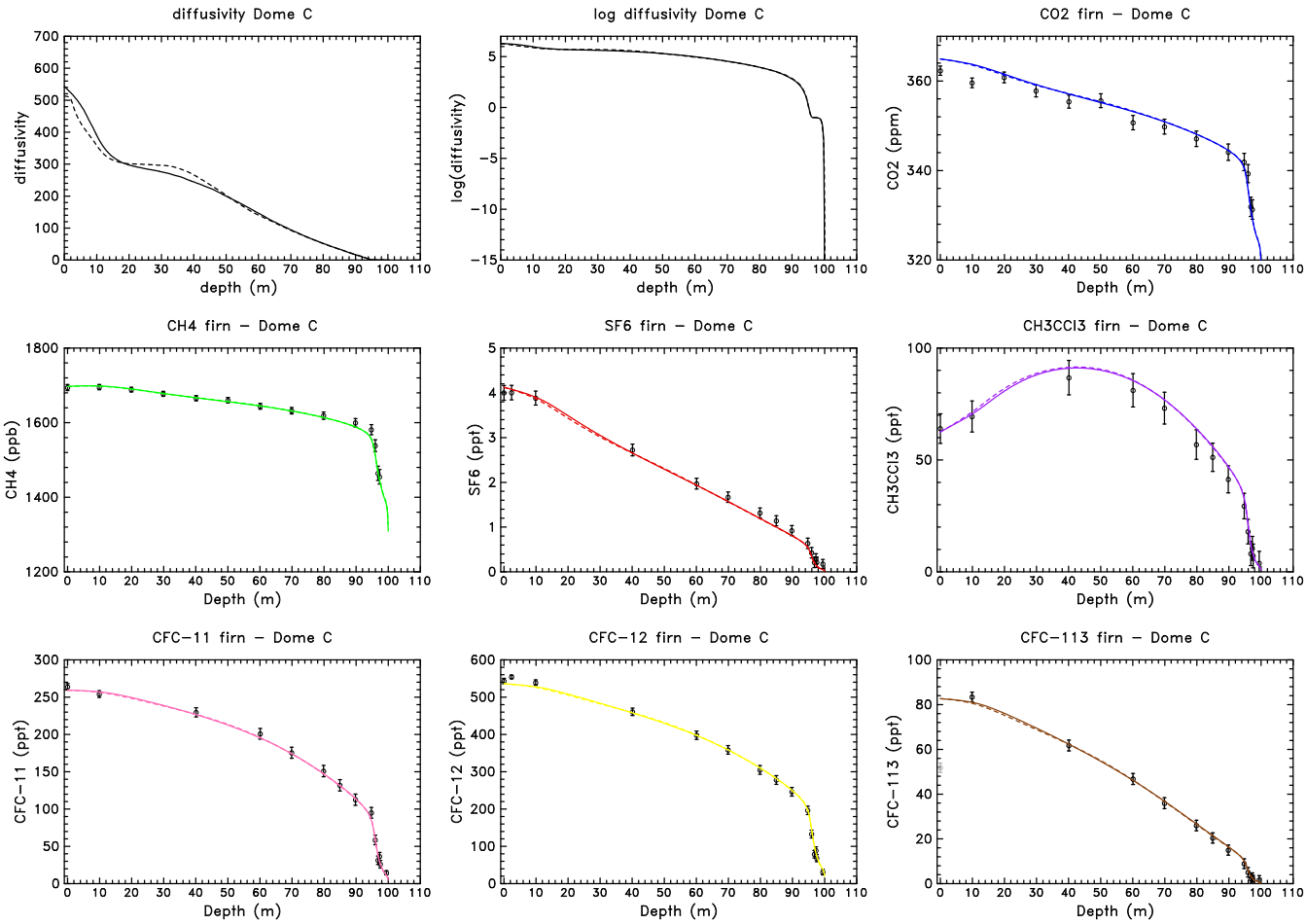

Fig. 18. Diffusivity (reduced to CO_2, in m^2/year) and gas mixing ratios at Dome C: parameterized initial diffusivity ('—') and zero initial diffusivity ('- - -').

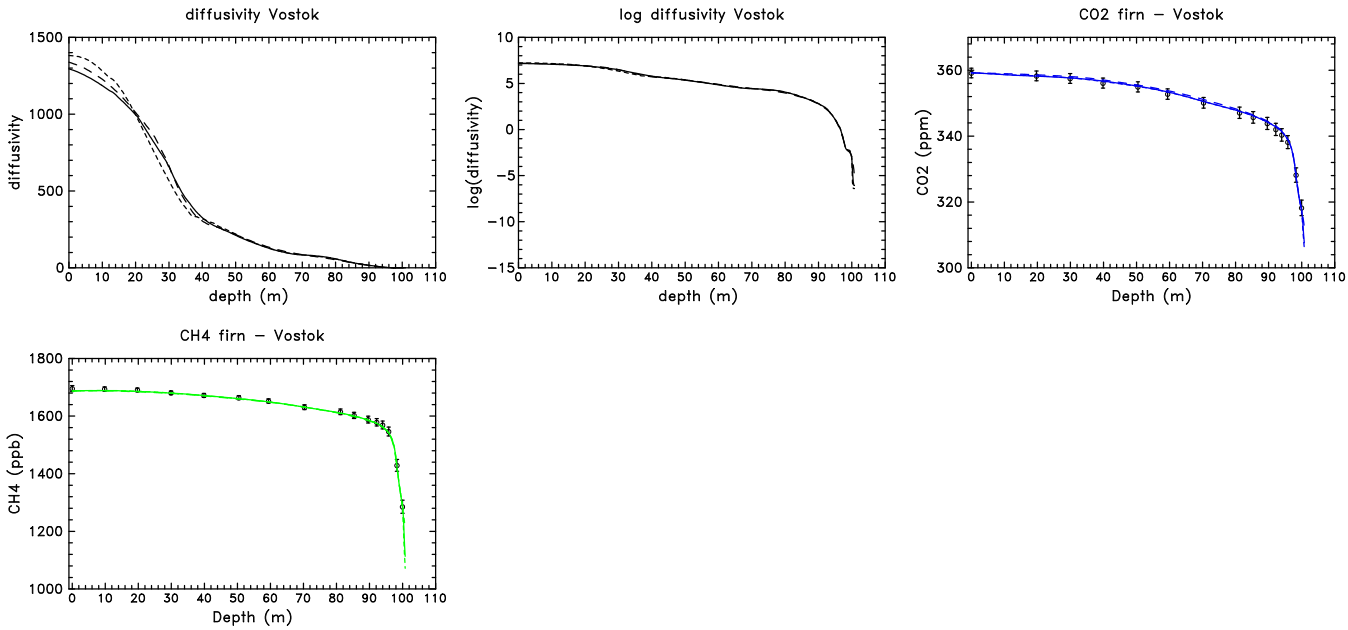

Fig. 19. Diffusivity (reduced to CO_2, in m^2/year) and gas mixing ratios at Vostok: parameterized initial diffusivity ('—'), zero initial diffusivity ('- - -') and starting gravitational settling at 0 m rather that 13m ('– – –').

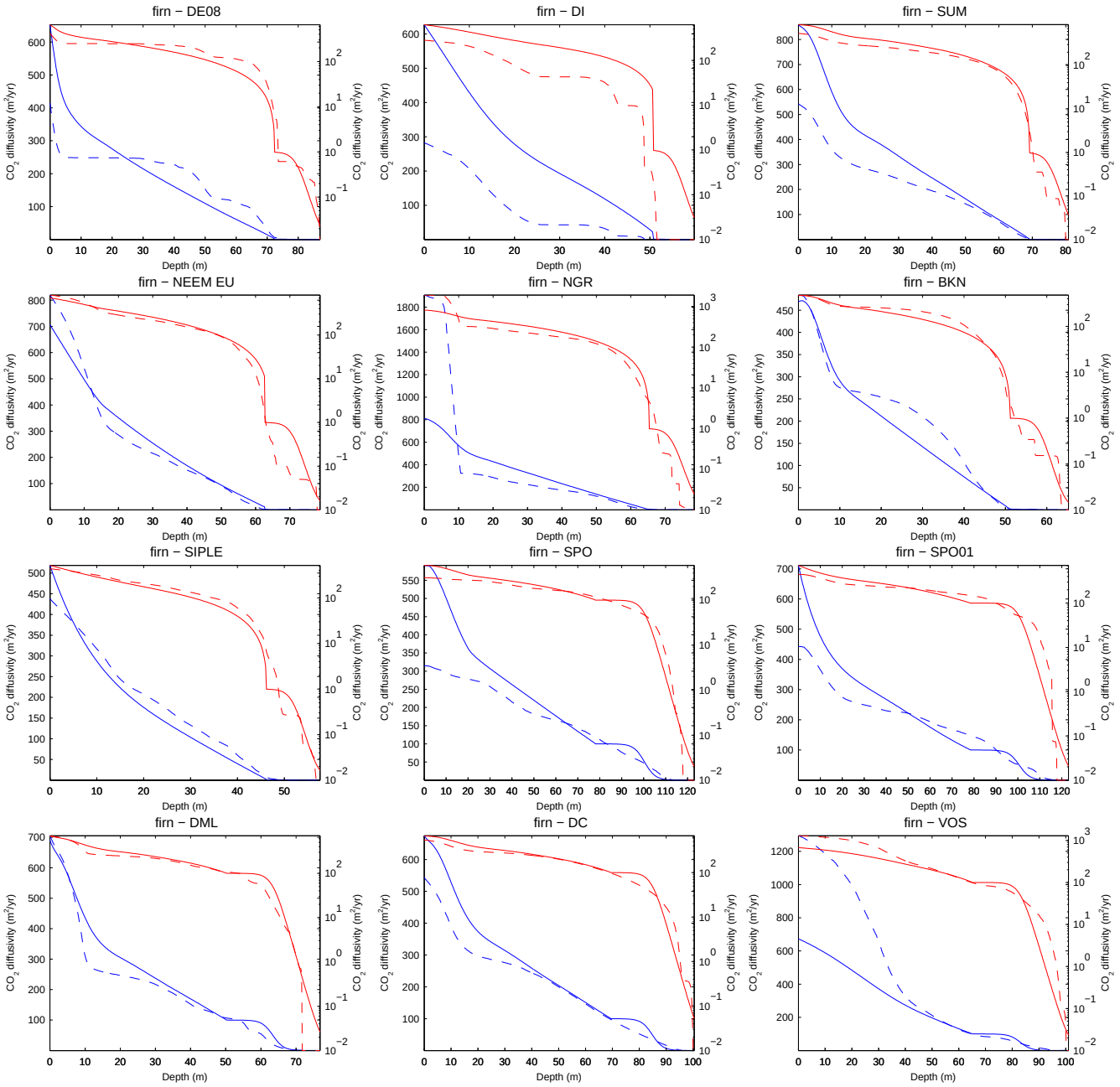

Fig. 20. Comparison between the optimum CO_2 diffusivity obtained from multi-gas data ('- - -') and the one obtained from the simple scaling law (Eqs. (21)-(22) in the main paper, '—'), presented in linear (blue) and log (red) scales.

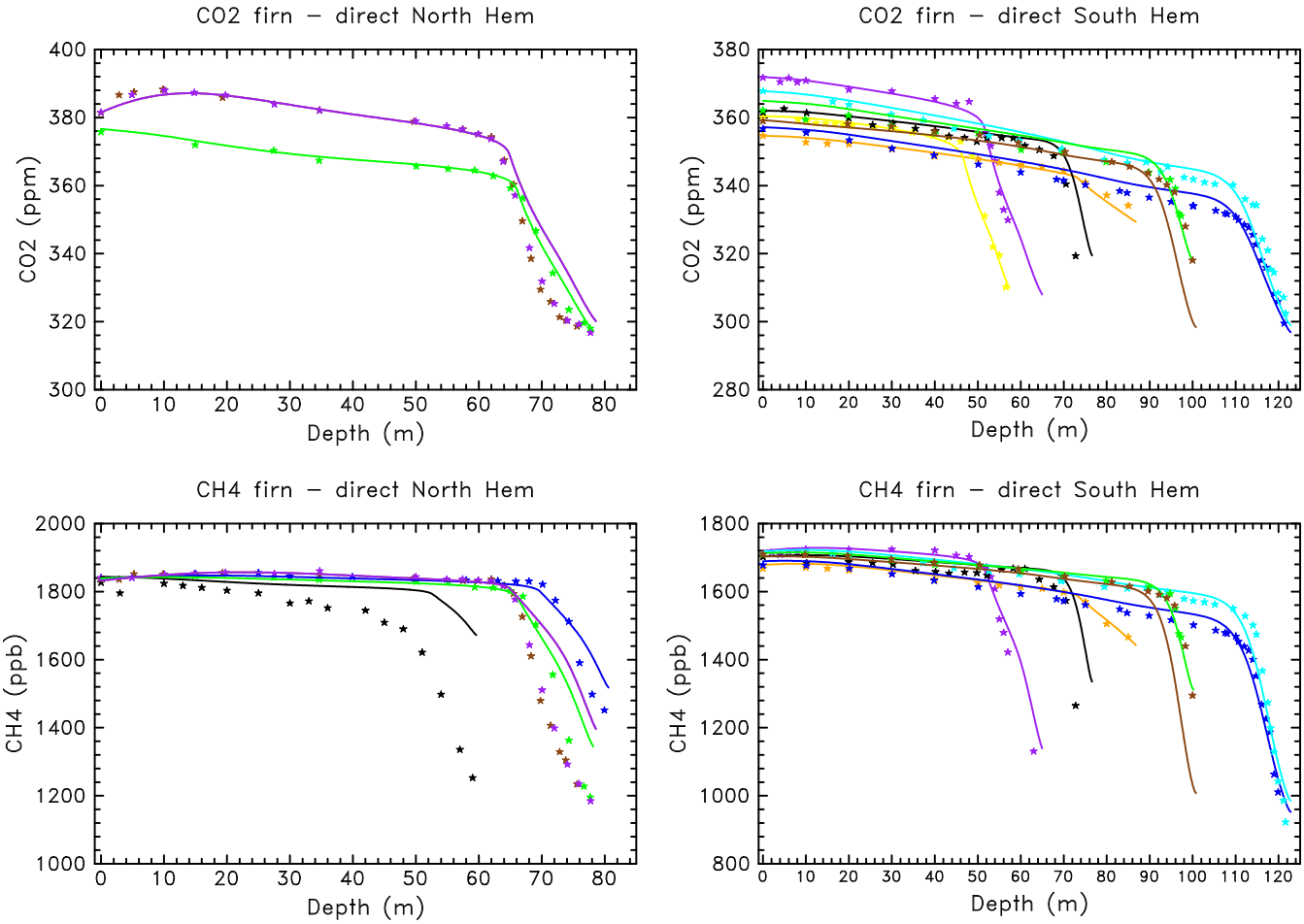

Fig. 21. Mixing ratios of CO_2 and CH_4 in firn calculated using the diffusivity obtained from the proposed scaling law. Arctic sites (left panels) are shown as: Devon Island in black, Summit in blue, NEEM in purple North GRIP in green. Antarctic sites (right panels) are shown as: DE08 in orange, Berkner in purple, Siple in yellow, South Pole 1995 in dark blue, South Pole 2001 in light blue, Dronning Maud Land in black, Dome C in green and Vostok in brown.